Université du Maine, Le Mans

Rapport de Synthèse
Présenté à l'Université du Maine, Le Mans
pour l'obtention de

l'Habilitation à Diriger des Recherches

par

Daniel CHATEIGNER
Maître de Conférences

Analyse Quantitative de Texture: un outil d'interprétation des propriétés anisotropes entre poudre et monocristal

ou

Quantitative Texture Analysis: a *Pot Pourri*

Soutenue le 15 Décembre 2000 devant le jury composé de:

A. Bulou	Professeur à l'Université du Maine, Le Mans
A. Gibaud	Professeur à l'Université du Maine, Le Mans
D. Grebille	Professeur à l'Université de Caen
A. Manceau	Directeur de Recherche au LGIT, Grenoble
M. Pernet	Professeur à l'Université J. Fourier, Grenoble
H.-R. Wenk	Professeur à l'Université de Californie, Berkeley

Laboratoire de Physique de l'Etat Condensé

à Magali

Remerciements

L'exercice de synthèse qui suit est une excellente opportunité pour faire le point d'environ 6 années d'activités post-doctorales. C'est aussi une entreprise qu'il convient de remettre à sa place pour ne pas qu'elle ait l'air trop égocentrique. Beaucoup de personnes ont participé à différents niveaux à ses travaux de recherche, qu'ils aient été directement impliqués ou simplement fourni la bonne humeur, l'amitié ou la connaissance. J'espère qu'ils se reconnaîtront s'ils n'apparaissent pas directement dans le texte, car il eut été impossible de les mentionner tous ici.

Aussi, qu'ils en soient chaleureusement remerciés, et en espérant que nos chemins se croiseront à nouveau à de multiples occasions.

Un acteur indirect mais non négligeable a contribué à faciliter ce travail, merci donc à l'existence du TGV ...

SOMMAIRE

Abréviations 1

1. INTRODUCTION 3
   1.1. Definition of the OD and usual methodology 5
   1.2. General problematics, limits 9
   1.3. Used experimental texture set-ups 27

2. RELIABILITY of the f(g) REFINEMENT
   2.1. Usual parameters 28
   2.2. Extensions 31

3. TEXTURE to PHYSICAL PROPERTIES CORRELATION
   3.1. Critical current density in thin films of Y-Ba-Cu-O 37
   3.2. Critical current density in mono- and multifilament tapes and wires of the Bi,Pb-Sr-Ca-Cu-O system 40
   3.3. Anionic conductivity in the Bi-Co-V-O system 52
   3.4. Remanent polarisation and pyroelectric coefficients in PTL and PTC films 59
   3.5. Magnetic properties of easy-axis and easy-plane magnetisation compounds 70
   3.6. Levitation forces in bulk melt-textured Y-Ba-Cu-O 79

4. TEXTURE EFFECTS on TECHNIQUES of ANALYSIS
   4.1 Polarised EXAFS spectroscopy 84
   4.2 Diffraction combined analysis 92

5. QTA of MOLLUSC SHELLS
   5.1. Aragonitic layers 112
   5.2. Calcitic layers 115

6. QTA APPROACH of POLYMERS 135

7 CONCLUSIONS and PERSPECTIVES

7.1. New optics of the goniometer 138

7.2. Laue orientation mapping 139

7.3. ESQUI project 140

References 142

Abréviations

ADC:	*Arbitrarily Defined Cells* méthode de résolution de l'OD
ALS:	*Advanced Light Source*
CEA:	Commissariat à l'Energie Atomique
CPS:	*Curved Position Sensitive detector*
CRETA:	Centre de Recherche d'Etudes et de Technologies Avancées, CNRS Grenoble
CRPAM:	Laboratoire mixte St Gobain-CNRS, Pont à Mousson
CRTBT:	Centre de Recherche sur les Très Basses Températures, Grenoble
CSIC:	*Consejo Superior de Investigaciones Cientificas of España*
CTTM:	Centre de Transfert de Technologie du Mans
DESC:	*Department of Earth Sciences, Cambridge University*, UK
DGGB:	*Department of Geology and Geophysics at Berkeley, University of California,* USA
DIM:	*Dipartimento di Ingegneria dei Materiali, Università di Trento*, I
DMF:	*Departamento de Materiales Ferroeléctricos* (CSIC-Madrid), E
DSTM:	*Dipartimento di Scienze della Terra*, Milano, I
EBSD:	*Electron Back Scattering Diffraction*
ENSIM:	Ecole Nationale Supérieure d'Ingénieurs du Mans
EPM-MATFORMAG:	Elaboration par Procédés Magnétiques, Matformag, CNRS Grenoble
ESRF:	*European Synchrotron Radiation Facility*
EXAFS:	*Extended X-ray Absorption Fluorescence Spectroscopy*
FDOC:	Fonction de Distribution des Orientations Cristallines
ICMA:	*Instituto de Ciencias de Materiales de Aragón*, Zaragoza, E
ILL:	Institut Laue-Langevin
IB-DEG:	*Institute of Biology, Dep. of Ecology & Genetics, University of Aarhus,* Denmark
INPG:	Institut National Polytechnique de Grenoble
LBGE:	Laboratoire de Biologie et Génétique Evolutive
LC:	Laboratoire de Cristallographie, CNRS Grenoble
LDF:	Laboratoire des Fluorures, Université du Maine, Le Mans
LEPES:	Laboratoire d'Etude des Propriétés Electroniques des Solides, CNRS Grenoble
LETI:	Laboratoire d'Electronique, de Technologie et d'Instrumentation, CEA Grenoble
LGIT:	Laboratoire de Géophysique Interne et Tectonophysique, CNRS Grenoble
LPCI:	Laboratoire de Polymères, Colloïdes, Interfaces, Le Mans
LPEC:	Laboratoire de Physique de l'Etat Condensé, Le Mans
LPMC:	Laboratoire de Physicochimie de la Matière Condensée, Montpellier
LURE:	Laboratoire pour l'Utilisation du Rayonnement Electromagnétique
MBE:	*Molecular Beam Epitaxy*

MEB:	Microscope Electronique à Balayage
MESR:	Ministère de l'Enseignement Supérieur et de la Recherche
OD or ODF:	*Orientation Distribution (Function)*
PSD:	*Position Sensitive Detector*
QTA:	*Quantitative Texture Analysis*
SCT:	*Siliceous Crust Type*
SINPC:	*Saha Institute of Nuclear Physics, Calcutta*, India
UM:	Université du Maine
WIMV:	méthode de détermination de l'OD, de Williams Imhof Matthies Vinel

Introduction

L'anisotropie des propriétés physiques macroscopiques d'un échantillon polycristallin ne peut être observée que si les cristallites de cet échantillon sont préférentiellement orientés. L'intérêt de l'analyse quantitative des orientations préférentielles (QTA) a joué un rôle primordial dans le passé, et encore aujourd'hui, par exemple pour optimiser les propriétés mécaniques d'alliages métalliques, pour comprendre les déformations mises en jeu dans certains phénomènes géophysiques ou pour limiter les pertes de matière lors de procédés industriels. Aussi, je passerai sous silence cet énorme travail, d'abord parce qu'il n'est pas dans mes centres d'intérêt actuel, ensuite parce que la littérature foisonne dans ce domaine [Kocks, Tomé and Wenk 1998].

Récemment, l'élaboration de matériaux aux propriétés physiques très anisotropes a relancé un intérêt croissant pour l'analyse texturale. C'est le cas pour les ferro et piézo-électriques, les supraconducteurs, les conducteurs ioniques, les matériaux composites, les polymères … L'utilisation de la diffraction (rayons X, neutrons et électrons) a aujourd'hui largement remplacé les anciennes méthodes pétrographiques (principalement microscopies optiques en lumière polarisée), qualitatives et souvent incomplètes:

- pour le calcul de certaines propriétés physiques macroscopiques, conséquences de tenseurs anisotropes (propriétés mécaniques, propagation anisotrope des ondes acoustiques, propriétés magnétiques), qui peuvent être modélisées en introduisant des données de QTA.
- pour comprendre la corrélation qui existe entre les tenseurs microscopiques et leur répercutions macroscopique dans des échantillons polycristallins texturés (piézo et ferroélectricité …)
- pour déterminer les modes de croissance (épitaxie ...), donc optimiser l'élaboration.

La limite de certaines techniques d'investigation structurale a aussi pu être repoussée grâce à l'incorporation des informations de QTA. Par exemple:

- en EXAFS, grâce à l'emploi combiné de l'EXAFS polarisé et de la QTA, pour atteindre des paramètres structuraux particuliers
- en couplant les analyses Rietveld et WIMV pour l'analyse combinée structure-texture-contraintes

- en analyse de texture elle-même, en utilisant les méthodes du profil complet pour l'étude de la texture de composés partiellement cristallisés ou turbostratiques,

Je décris ci-après les activités qui m'ont principalement occupé depuis 1995, et qui me paraissent représenter la démarche qui motive mes recherches. Certaines parties de ces travaux sont en cours, je présente l'état actuel de leurs développements. Les travaux déjà finalisés apparaissent sous forme de publications. Je me suis permis d'écrire en langue anglaise l'ensemble du texte de ce rapport de synthèse, pour gagner en homogénéité avec les publications insérées, et pour permettre que ce travail puisse aussi servir à mes collègues et collaborateurs non francophones.

1. Introduction

1.1.: Definition of the ODF and usual methodology

The quantitative determination of the texture is based on the concept of Orientation Distribution Function, f(g), which represents the statistical distribution of the orientations of the constitutive crystals (crystallites) in a polycrystalline aggregate:

$$\frac{dV(g)}{V} = \frac{1}{8\pi^2} f(g)\, dg \qquad (1)$$

where $dg = \sin(\beta) d\beta d\alpha d\gamma$ is the orientation element, defined by three Euler angles $g=\alpha,\beta,\gamma$ (Figure 1) in the orientation space (or G-space), that bring a given crystal co-ordinate system K_B co-linear with the sample co-ordinate system K_A=(**X,Y,Z**), or (**100**, **010**, **001**). The G-space can be constructed from the space groups, taking into account their rotation parts and the inversion centre. The two first angles α and β determine generally the orientation of the $[001]^*$ crystallite direction in K_A, they are called azimuth and colatitude (or pole distance) respectively. The third angle, γ, defines the location of another crystallographic direction, chosen as [010] (in the (a,b) plane or orthogonal crystal cells). V is the irradiated volume (if one uses diffraction experiments) of the sample, dV(g) the volume of crystallites which orientation is between g and g+dg.

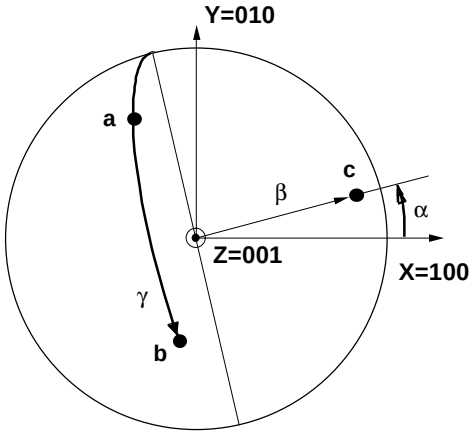

Figure 1: Definition of the three Euler angles that define the position of the crystallite co-ordinate system K_B=(**a**,**b**,**c**) of an orthogonal crystal cell in the sample co-ordinate system K_A=(**X**,**Y**,**Z**). Note, **100**, **010** and **001** are not Miller indices but vectors referring to an ortho-normal frame aligned with K_A

The function f(g) then represents the volumic density of crystallites oriented in dg. It is measured in m.r.d. (multiple of random distribution) and normalised to the value $f_r(g)=1$ for a sample without any preferred orientation (or random). The function f(g) can take values from 0 (absence of crystallites oriented in dg around g) to infinity (for some of the G-space values of single crystals).

The normalisation condition of f(g) over the whole orientation space is expressed by:

$$\int_{\alpha=0}^{2\pi}\int_{\beta=0}^{\pi/2}\int_{\gamma=0}^{2\pi} f(g)\,dg = 8\pi^2 \qquad (2)$$

Experimental measurements are the so-called pole figures, $P_{\mathbf{h}}(\mathbf{y})$, with $\mathbf{h}=<hkl>^*$ and $\mathbf{y}=(\varphi,\vartheta)$, always incomplete in some way. They determine the distribution of the normals <hkl>* to the crystallographic planes {hkl} which are diffracting for the (φ,ϑ) orientation of the sample in the diffractometer frame. For one pole figure, φ and ϑ are varied in order to cover the maximum range of orientations. However, one pole figure is only a measure of the distribution of one direction type <hkl>*, a rotation around it ($\tilde{\varphi}$ angle) giving the same diffracted intensity. This can be expressed by:

$$\frac{dV(\varphi\vartheta)}{V} = \frac{1}{4\pi} P_{\mathbf{h}}(\varphi\vartheta)\sin\vartheta d\vartheta d\varphi \qquad (3)$$

and similarly to the OD, every pole figure of a random sample will have the same density $P_{\mathbf{h}}(\mathbf{y})=1$m.r.d.. Lets mention at this step that the pole figures obtained using normal diffraction methods are the so-called reduced ones, $\widetilde{P}_{\mathbf{h}}(\mathbf{y})$. The Friedel's law makes that the measured pole figures are superpositions of +**h** and -**h** true pole figures. The fact that for normal diffraction (and for centrosymmetric crystal systems even for anomalous scattering too) only reduced pole figures can be measured is known for texturologists as 'ghost' phenomena [Matthies et Vinel 1982, Matthies, Vinel et Helming 1987]. We will not take account of this here since the ghost suppression, if possible, would need anomalous diffraction and very intense beams. Instead, theoretically derived ghost-correcting approximations will be used.

The normalisation of the pole figures is, similarly as in (2), operated through:

$$\int_{\varphi=0}^{2\pi}\int_{\vartheta=0}^{\pi/2} P_{\mathbf{h}}(\varphi\vartheta)\sin\vartheta\, d\vartheta d\varphi = 4\pi \qquad (4)$$

Following Equations (1) and (2), one can obtain the fundamental equation of texture analysis:

$$P_{\mathbf{h}}(\mathbf{y}) = \frac{1}{2\pi}\int_{\mathbf{h}//\mathbf{y}} f(g)\, d\tilde{\varphi} \qquad (5)$$

This equation was solved several years ago by Bunge, using generalised spherical harmonics formulation [Bunge et Esling 1982, Bunge 1982], but only in the case of high crystal symmetries. It qualitatively looks as neglecting the reduction problem and crystal-symmetry related sums over all physically equivalent **h** for a given type of (hkl) planes. Furthermore, the reduced diffraction pole figures only access the even orders of the harmonics, which gives rise to the 'ghost' phenomena [Matthies 1979, Matthies et Vinel 1982] undesirable for a quantitative description of f(g). An approximative "ghost correction" by creating the odd orders is very complicated in the harmonic apparatus [Esling, Muller et Bunge 1982]. Also, for strongly textured samples, the harmonics formulation proved to be less adequate than the discrete methods [Ruer 1976, Vadon 1981, Imhof 1982, Matthies, Wenk et Vinel 1988, Pawlik 1993]. One advantage was originally that it provides the necessary material for the simplest approximation of the mechanical property simulations with a limited number of coefficients (the harmonic coefficients in fact), that can now be computed from the Orientation Distributions as calculated with discrete methods. A philosophical disadvantage of the method is that it assumes a particular shape of the distributions, the one that corresponds to a harmonic analytical formulation, whereas it does not correspond in all cases to a real physical description. This is why in this text f(g) refers to the Orientation Distribution (or OD) of the crystallites instead of the Orientation Distribution Function (or ODF) of many texture books. An exact solution of (5) in an analytical closed form without any series expansion was given [Matthies 1979], which permits, in a systematic way, to analyse the properties of the ghosts and to develop reasonable ghost correcting algorithms.
The so-called "vector" [Vadon 1981] and ADC [Pawlik 1993] methods have not been used in this work. We did not use the vector method because it has not been developed to low symmetry materials which is of our interests here. The ADC method would be interesting to practice on our data, though it has been compared by Wenk et al. (1994) on materials with a

relatively low texture strength and did not show neither better nor worse results than the WIMV algorithm.

We then used the iterative approach WIMV [Matthies et Vinel 1982, Matthies et Wenk 1985] for the refinement of the OD. This method ensures a conditional ghost correction and quantitative analysis down to the triclinic crystal symmetry and is calculated for a triclinic texture symmetry. It is based on the numerical refinement of f(g):

$$f^{n+1}(g) = N\left[\frac{f^{n}(g)f^{0}(g)}{\prod_{hkl}\left(\mathrm{P}_{\mathbf{h}}^{\mathrm{n}}(\mathbf{y})\right)^{\frac{1}{I}}}\right] \qquad (6)$$

where the product extents over the I experimentally measured pole figures, $f^{n}(g)$ and $\mathrm{P}_{\mathbf{h}}^{\mathrm{n}}(\mathbf{y})$ represent the refined values of f(g) and $\mathrm{P}_{\mathbf{h}}^{\mathrm{n}}(\mathbf{y})$ at the n^{th} step respectively. The number N is a normalising factor. The $\mathrm{P}_{\mathbf{h}}^{\mathrm{n}}(\mathbf{y})$ values are calculated at each cycle with Eq. (5).

The best solution found for f(g) is for the minimum averaged reliability factors:

$$\overline{RP}_{x} = \frac{1}{I}\sum_{i}\sum_{j}\frac{\left|P_{\mathrm{h_i}}^{calc}(\mathbf{y}_j) - P_{\mathrm{h_{ii}}}^{obs}(\mathbf{y}_j)\right|}{P_{\mathrm{h}_i}^{obc}(\mathbf{y}_j)} \qquad (7)$$

where j is for all **y** experimental values, i varies from 1 to I the number of pole figures, obs and calc refer respectively to the observed and recalculated (from the OD) pole densities. The value x is a criterion used to appreciate the quality of the refinement for the low and high density levels. We use x=0.05 to reveal the global quality and x=1 to show this quality for the density values higher than 1m.r.d..

Once f(g) is satisfactorily obtained, one can calculate factors which give an estimate of the texture strength. Caution should be taken here when comparing samples on the base of overall texture strength parameters. Samples should have the same crystal symmetry and exhibit similar texture components. The first texture strength parameter is the so-called 'texture index' [Bunge 1982] (expressed in m.r.d.^{2}):

$$F^2 = \frac{1}{8\pi^2} \sum_i [f(g_i)]^2 \Delta g_i \qquad (8)$$

with $\Delta g_i = \sin\beta_i \Delta\beta\Delta\alpha\Delta\gamma$ is the OD cell volume.

The second parameter that we are using is a measure of the texture disorder, evaluated by the calculation of the entropy:

$$S = \frac{1}{8\pi^2} \sum_i f(g_i) \ln f(g_i) \Delta g_i \qquad (9)$$

Entropy and texture index are correlated, but it is not possible to obtain an analytical expression for this correlation.

1.2.: General problematic, limits

Here comes the problem of the pole figure measurements, which has to be adapted to the samples to characterise. It started originally [Schulz 1949a et 1949b] with the use of a 4-circle diffractometer equipped with a point detector, and using a filtered (only) radiation. It became recently a necessity to use also a purer radiation as delivered by a monochromator [Wenk 1992], which was fairly new in the texturologists world. But one of the main problems still remained. One had to measure every single pole figure one after each other, doing the same $\chi\varphi$-scan for each of them. One way to avoid this time-consuming measurement was to build systems with more intense fluxes, as one can have using rotating anodes generators [Chateigner et al. 1997] or synchrotrons [Wenk et al. 1997]. Another way was to use multidetectors, usable on classical generators, like position sensitive (PSD), curved position sensitive (CPS) or 2-dimensional detectors (image plates or CCDs). The first use of position sensitive detectors was developed using neutron radiation [Bunge, Wenk et Pannetier 1982], were experimental time can be a crucial parameter. In this way, we demonstrated that quite a lot of the experimental time can be saved, also with a limited range in the pole figure coverage [Chateigner, Wenk et Pernet 1997]. Using this approach the 5°x5° grid of the rotation around diffractometer axes are in some way deformed in the resulting pole figures [Heizmann et Laruelle 1986], after the localisation corrections. The ideal would be to measure those points that, after correction, result in a non-distorted 5°x5° coverage of the pole figure. However, for one incidence angle, this is feasible only for one of the pole figures, and

whatever the grid used. And if several incidences are measured, the experiment needs more time and the use of a PSD becomes less interesting. The way to get rid of this deformation is to spline-interpolate the experimental points and recreate a non-distorted grid. All what is mentioned here is also true for an hexagonal grid [Matthies et Wenk 1992].

This time-saving methodology is presented in the following paper. It presents also how to operate a complete analysis, from scratch data.

But another interest in using PSDs is revealed when the peak position or peak profile is of interest. When internal stresses exist in the studied material, the peak position moves when the tilt angle changes, precluding any reliable measurement of the texture with a point detector, particularly if dealing with a well crystallised material for which diffraction peaks have low FWHMs.

On the other hand, for micro- or partially crystallised materials, peaks are so much broadened that some questions should be pointed out when working with a point detector:

- what are the relative contributions of each of the peaks inside the detector ?
- what will be these contributions with the occurrence of defocusing ?
- is the detector position representative of all the crystallites (or which part of the irradiated volume does it concern) ?
- how much the diffracted signal is perturbated by the amorphous contribution ?

Figure 2 is an example of a polypropylene diagram that exemplifies how these problems could perturbate the results.

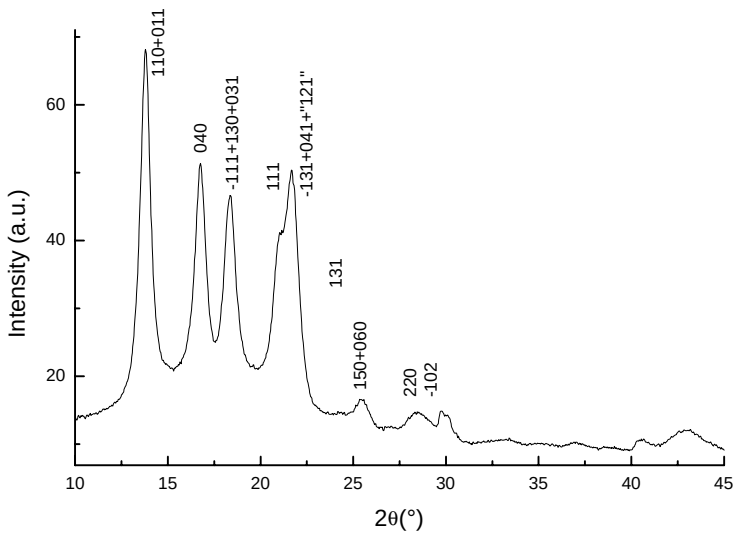

Figure 2: Example of an x-ray diffraction diagram for a plasma-treated polypropylene film.

There are actually three different manners to handle such a problematic analysis, all using a CPS or a PSD. The less elegant, and also less reliable, is to process a direct numerical integration of the peaks with background and amorphous subtraction using a linear interpolation. Since the amorphous part does not evolve linearly, it creates artefacts that act as a random contribution in the pole figures. This method should still be restricted to fully crystallised materials, for which it works nicely.

The second approach, that we used to treat this sample, is to fit independent peaks with convenient shapes either in a whole pattern fitting procedure or on separated peaks or groups of peaks, versus the sample orientation. In this methodology, background and amorphous signals are subtracted with another fitted function. Of course this approach assumes that the structure is perfectly known which is not always the case, but was shown to be able to provide ODs of polyphase materials.

The most elegant way at the present time is to resolve the structure and the texture in a combined approach as now developed for few years using TOF [Wenk, Matthies et Lutterotti 1994; Matthies, Lutterotti et Wenk 1997] and monocinetic [see § 4.2.] neutron investigations. This approach is now quite updated with x-rays, but still needs an effort for the corrections and calibration of the microstructural parameters.

1.3. Used experimental texture set-ups

In this part, it would have been boring to get into too much instrumental details. They can however be found in the corresponding papers.

Parts of the mentioned studies have been based on measurements operated with point detectors using 4-circles diffractometers (Dosophatex at LC-Grenoble, Seifert at LC-Grenoble, Huber at DGGB-Berkeley), on samples with well separated or fully overlapped peaks.

When texture was needed at a cm^3 level, neutron scattering was used, at the D1B-ILL and D20-ILL diffractometers, though with a CPS.

We also tried to measure some shells with EBSD at DGGB-Berkeley, we will discuss briefly these experiments.

The rest of the experiments presented here have been measured at LPEC with a new diffractometer set-up using the CPS 120 of INEL inc. presented in Figure 3.

Since at the time of the papers, no algorithm was available to treat the OD from highly resolved data (like 1°x1° grids), the examples of very strongly textured samples were treated using direct normalisation [Chateigner 1994]. In other cases, data treatments were operated within the BEARTEX package [Wenk et al. 1998].

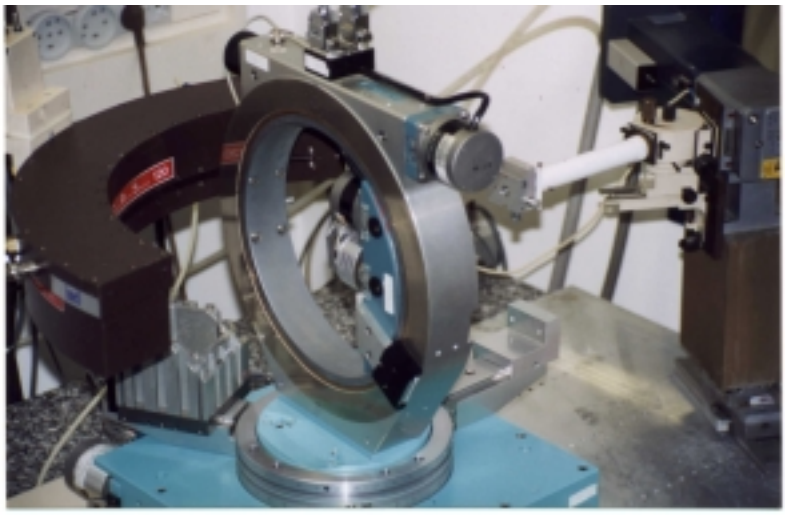

Figure 3: The x-ray diffractometer as set-up at LPEC

2. Reliability of the f(g) refinement

2.1. Usual parameters

If the RP factors are suitable for the refinement itself, they depend on the texture strength since they are not weighted by the density level, and consequently make the comparison of refinement's quality between samples somehow ambiguous. In other words, one should compare the refinement quality with RP factors, only for similar texture strengths. This is tendentious, particularly for highly textured samples (with large RP values), since the WIMV method relies on an entropy-maximisation related algorithm.

Figure 4 shows how the RP_0 and RP_1 factors are varying with the texture strength. This diagram results of approximately hundred OD refinements including all crystal symmetries, from measurements taken with four different diffractometers (LC, DGGB, D1B-ILL, LPEC), and which can be found in the cited literature. Of course, there are dispersions of the points, since they depend on the quality of the measurement. In this study, since the OD is calculated on the base of a discrete measurement of 5°x5°, one cannot expect to quantitatively determine textures with FWHM of the dispersion smaller than 5° at minimum. The Beartex texture package recommends in fact 7.5°. We took this latter limit in Figure 4a, which corresponds to a texture index around 300 m.r.d.^{2} on average. As one can see, both RPs (as defined by Equation (7)) evolve with the texture strength, in a similar manner. This variation conserves the same global shape at smaller texture strengths (4b), and apparently does not depend on the crystal structure (in the resolution of our experiments).

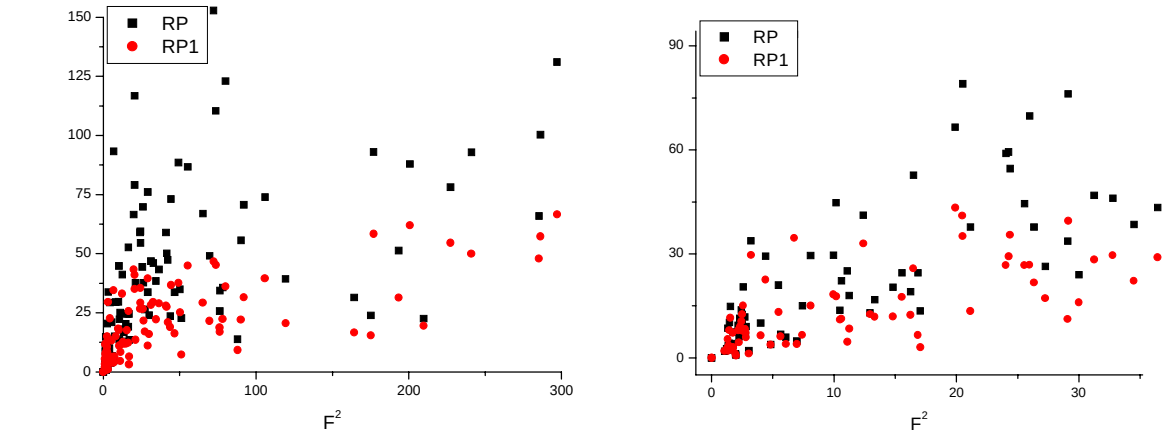

a) **b)**

Figure 4: variation of the experimental RP factors with, and for two different ranges of F^2.

We decided to test the theoretical limit that one can reach using the WIMV technique and a 5°x5° scan grid, on modelled components with Gaussian shapes of varying FWHMs (Table 1). We chose to use a cubic crystal symmetry with one texture component g=(0,0,0) (Figure 5a), and to refine the OD on the model {110} complete pole figure. The refinement process was stopped when a convergence velocity of 0.1 was reached, or when the RP_0 factor was larger than for the just previous cycle. Figure 5b shows the RP evolution of the modelled texture with the texture strength. Since the refinement is done on noiseless distributions, the RPs are correspondingly lowered.

But it is clearly seen that RP values are increasing with F^2 also for modelled components, which means that the WIMV algorithm has some difficulties to reproduce textures when the width of the dispersion becomes close to the experimental resolution related to the scan grid. It would be interesting to compare these results with the sensitivity to experimental resolution of other discrete methods like ADC. In Figure 5, the modulation observed between RP_0 and RP_1 factors is due to the choice of the exponent parameter (Table 1) which has to be modified, depending also on F^2, in order to better fit experimental data. This parameter may also be fitted, but we chose here to vary it by steps of 0.5 in the [0.5-2.5] range, and conserved the results for the lower RP_0.

The sensitivity of the WIMV algorithm to measurement resolution is included in the evolutions of the RPs obtained from real experiments as presented in Figure 4. In these experiments the resolution-sensitivity of the method is combined to the true experimental reliability, in a way which is not perfectly understood at the present time, and ideally should be removed. We may imagine calibration processes to correct for the sensitivity of the algorithm, but in absence of a real physical or statistical fundament. We will propose another alternative in the following, which tends to minimise the intrinsic sensitivity of the R-factors to the magnitude of the scattered signal.

We should first place a limit value of the FWHM of the dispersion, the one that corresponds to an unacceptable difference between the experiment and the model. If one accepts a maximum of 10% on the RP_1 values, then a 8.5° dispersion appears as the strongest texture refinable in this modelled texture type. This value corresponds to a maximum F^2 of 300 m.r.d.^{2} approximately.

F^2 (m.r.d.^{2})	RP_1 (%)	RP_0 (%)	FWHM (°)	- S	Cyc.	{110} dif. (m.r.d.)	Exp.
1	0.27	0.4	90	0	2	0	2
1.1	0.68	1.15	60	0.05	17	0	2
1.92	0.92	1.78	45	0.36	28	0.01	2
4.15	1.64	3.21	35	0.94	36	0.05	2
11.56	3.07	6.38	25	1.92	24	0.08	2
23.21	5.03	6.29	20	2.64	27	0.12	2
56.89	7.43	8.9	15	3.51	17	0.29	0.5
69.48	7.08	9.41	14	3.7	6	0.41	0.5
112.05	7.86	11.09	12	4.18	8	0.7	0.5
199.8	6.82	13.59	10	4.75	16	1.42	0.5
285.05	7.46	15.15	9	5.08	11	3.07	0.5
431.91	11.07	18.21	8	5.44	15	4.63	0.5
704.35	17.75	15.79	7	5.87	12	7.48	0.5
--	22.89	28.39	6.9	6.4	5	14.1	0.5

Table 1: Parameters resulting from the refinement of the OD of modelled texture components with variable FWHMs. Cyc.: number of cycles for stopping the refinement. Exp.: exponent parameter entering the convergence speed. {110} dif.: difference in maximum density between observed and recalculated {110} pole figure.

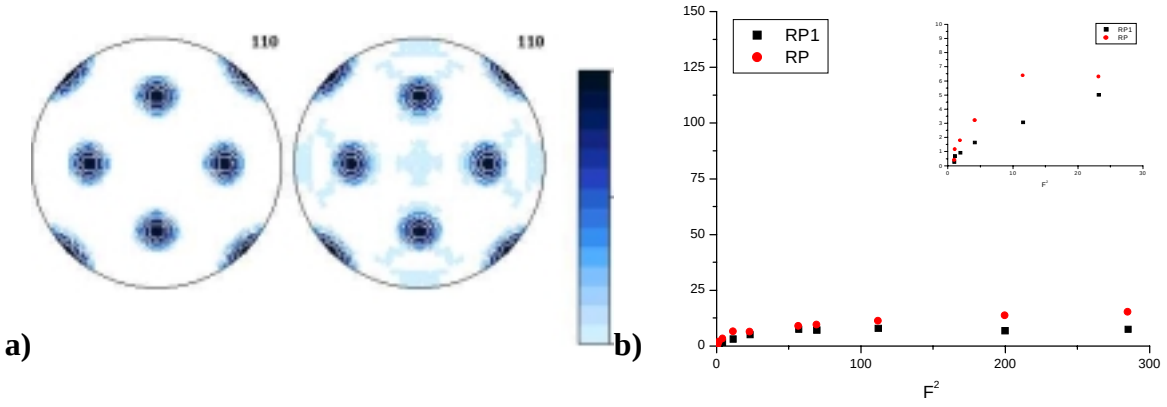

Figure 5: a): Simulated and recalculated {110} pole figure of a cubic crystal system in the g=(0,0,0) orientation (logarithmic density scale, equal area projection, max=52 m.r.d., min=0) and **b):** variation of the corresponding RP factors with F^2.

2.2. Extensions

Matthies, Vinel & Helming (1987) proposed reliability factors weighted by the surface area of the measured cells **y** of the pole figures. The surface-weighted averaged factors are calculated on the base of the pole densities by:

$$\overline{RP}_{Sx} = \sum_{i=1}^{I} \frac{\sum_{j=1}^{J} S_j \left| P^o_{\mathbf{h}_i}(\mathbf{y}_j) - P^c_{\mathbf{h}_i}(\mathbf{y}_j) \right| \theta\left(x, P^o_{\mathbf{h}_i}(\mathbf{y}_j)\right)}{\sum_{j=1}^{J} S_j P^o_{\mathbf{h}_i}(\mathbf{y}_j)} \qquad (10)$$

where:

$\mathbf{h}_i = (hkl)_i$; i = (1..I) Measured pole figures

$\mathbf{y}_j = (\alpha,\beta)_j$; j = (1..J) Measured points of the pole figures

$$\begin{cases} o : \text{observed normalised} \\ c : \text{WIMV - recalculated normalised} \end{cases}$$

$P_{\mathbf{h}_i}(\mathbf{y}_j)$: Pole density at $\mathbf{y}_j$ on pole figure $\mathbf{h}_i$

$I_{\mathbf{h}_i}(\mathbf{y}_j) = P_{\mathbf{h}_i}(\mathbf{y}_j) \cdot N_{\mathbf{h}_i}$: Corresponding diffracted intensity (11)

$N_{\mathbf{h}_i}$: Refined normalising factor

$w_{ij} = \frac{1}{\sqrt{I_{\mathbf{h}_i}(\mathbf{y}_j)}}$: Diffracted intensity weight

$S_j = \Delta\alpha\left[\cos\left(\beta_j - \frac{\Delta\beta}{2}\right) - \cos\left(\beta_j + \frac{\Delta\beta}{2}\right)\right]$; $S_0 = \pi\left(1 - \frac{\Delta\beta}{2}\right)$: Surface element for $\mathbf{y}_j$

$$\theta(x,t) = \begin{cases} 1 \text{ for } P_{\mathbf{h}_i}(\mathbf{y}_j) > x \\ 0 \text{ for } P_{\mathbf{h}_i}(\mathbf{y}_j) \le x \end{cases}$$

x = 0, ε, 1, 10 ...: criterion to estimate accuracy versus density level.

The calculations are based on experimental and WIMV-recalculated normalised pole figures (as delivered by BEARTEX) in Pofint [http://qta.ensicaen.ismra.fr/pofint]. Since the

weighting factors depend on the square root of the measured intensities (not the densities), we use the normalising factors from the WIMV refinement in order to first transform all densities into intensities. Also, the reliability factors (R-factors) will be calculated always relative to the observed values.

Results with surface-weighted factors for the same experiments as in Figure 4a are represented in Figure 6. Clearly the extent of the variation is less than for RPs, proving the efficiency of the weighting process, particularly for the higher texture strengths.

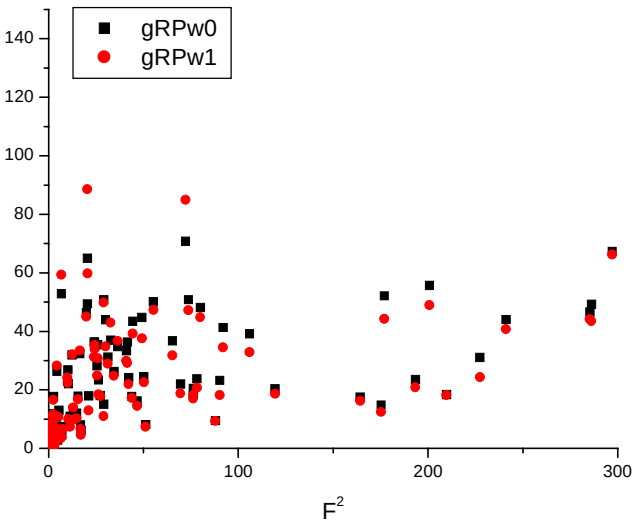

Figure 6: variation with F^2 of the surface-weighted RPw factors.

We will now introduce other weighted factors, and compare them to the previous ones on the base of our experiments.

Another R-factor is interesting to be calculated, since it corresponds to the Bragg R-factor of the Rietvelders (in powder crystal structure determination). We then call it the Bragg standard deviation factor:

$$\overline{RB}_x^2 = \sum_{i=1}^{I} \frac{\sum_{j=1}^{J} \left| I_{\mathbf{h}_i}^o(\mathbf{y}_j) - I_{\mathbf{h}_i}^c(\mathbf{y}_j) \right|^2 \theta\left(x, P_{\mathbf{h}_i}^o(\mathbf{y}_j)\right)}{\sum_{j=1}^{J} I_{\mathbf{h}_i}^o(\mathbf{y}_j)^2} \qquad (12)$$

which also would stand if one replaces intensities by pole densities, since the normalising factor simplifies in the expression. The Bragg R-factors could also be weighted using the surface elements (RBw), in the same way as the usual RP factors. Figure 7 shows the evolution of the Bragg surface-weighted R-factors with F^2. RBws exhibit roughly the same tendency as RPws.

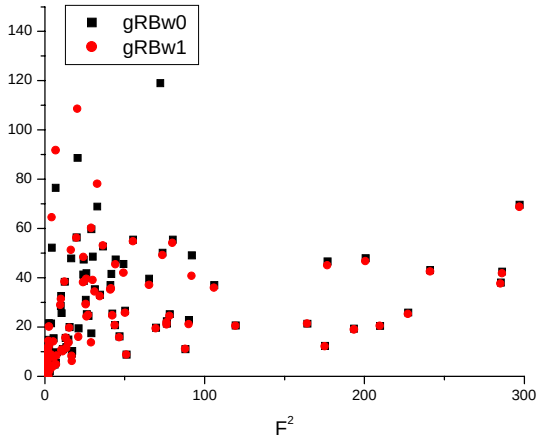

Figure 7: variation of the Bragg surface-weighted factors with F^2.

The Rietveld-like R-factor or "intensity-weighted" which takes into account the normal Gaussian distribution standard deviation (Eq. 13) for each measured intensity, even shows less overall variation with F^2 (Figure 8). We think it could be a better indicator of the OD refinement reliability.

$$\overline{Rw}_x^2 = \sum_{i=1}^{I} \frac{\sum_{j=1}^{J} \left| w_{ij}^{o} I_{\mathbf{h}_i}^{o}(\mathbf{y}_j) - w_{ij}^{c} I_{\mathbf{h}_i}^{c}(\mathbf{y}_j) \right|^2 \theta\left(x, P_{\mathbf{h}_i}^{o}(\mathbf{y}_j)\right)}{\sum_{j=1}^{J} w_{ij}^{o} I_{\mathbf{h}_i}^{o}(\mathbf{y}_j)^2} \qquad (13)$$

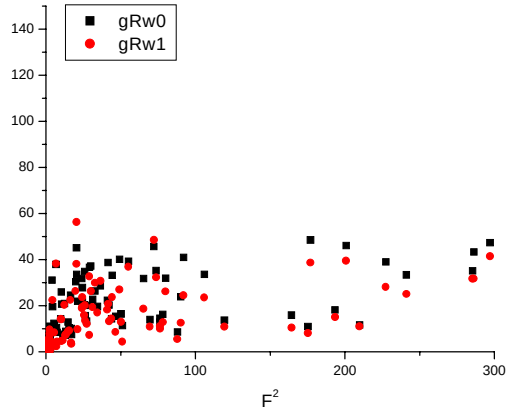

Figure 8: variation of the intensity-weighted R-factors with F^2.

It is not either clear if the different density levels are equally represented by the R-factors. This representativity of the densities in the R-factors is illustrated on $R_1(R_0)$ graphs (Figure 9), on which an equal-representativity lies on a 45°-line (straight line on the figures). The RP factors are deviating from this line, with relatively small RP_1s. It should be mentioned that this feature is not corresponding to a tendency of the WIMV techniques to favour high density levels, since the other R-factors do not show the same behaviour. It means on the contrary that the RP_0 gives more importance to the differences in low density levels than RP_1 does for the levels above 1 m.r.d.. This behaviour is also observed for the other non-weighted factor RB (not shown here), but quite disappears for all the weighted ones (RPw, RBw and Rw), RBw being the most regular. There is also a larger dispersion of the points in the case of RPs than for all others, and we retrieve a smaller strength dependence of Rws which are located closer to the origin than other factors.

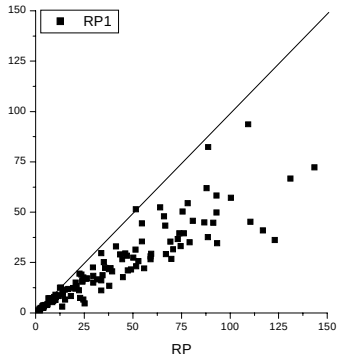

a)

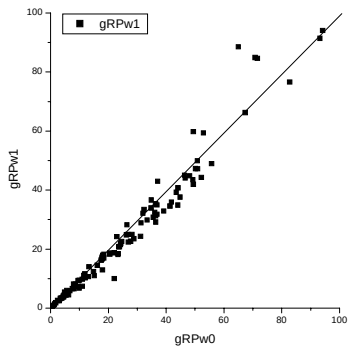

b)

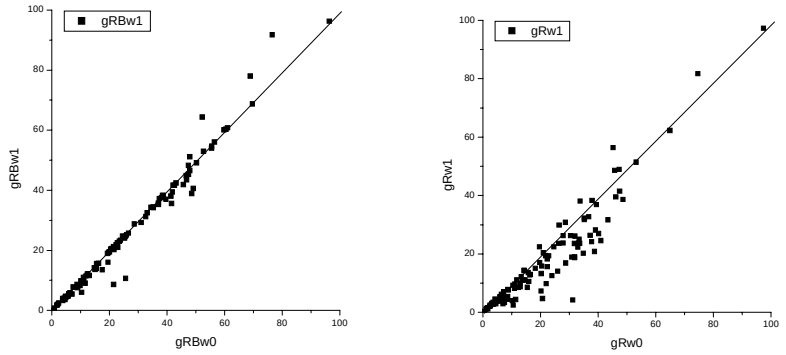

c) **d)**

Figure 9: Representativity of two different density level populations by the R-factors. **a):** RP, **b):** RPw, **c):** RBw, **d):** Rw

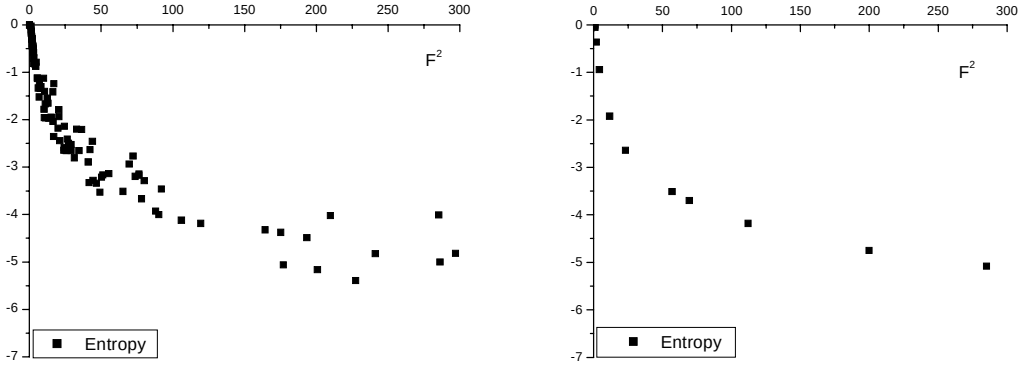

a) **b)**

Figure 10: Entropy variation with Texture index. **a):** for real samples, **b):** for modelled textures

This reliability analysis may also provide some criterion to test the goodness of the OD refinement. For one texture analysis, one point in Figures 9, we can appreciate if the refinement has been operated in a subjective manner: if the corresponding point is not placed on the 45° line on weighted factor plots, the operator has probably focused on part of the details of the analysis without considering the others. In certain cases this may be reasonable, but has to be justified. For instance, on the Rw graph (Figure 9d), one can observe points that are under the 45° line. Those have been obtained on a series of heteroepitaxial films with multiple heteroepitaxial relationships. The operator then put his interest in identifying the major texture components, giving importance to the RP_1 factors during the OD refinement.

Another test is available using these data, if we consider the modelled texture results as the best that one can reach. Looking at the variation of the entropy with the texture index (Figure 10b), modelled textures will be placed on a single line, which represents the solution for f(g) of (8) = (9). Comparing real experiments (Figure 10a) with modelled textures (Figure

10b) will help in identifying one refinement that may be ameliorated. Lastly, from Figures 10, one can experimentally see the relative evolutions of the texture strength parameters, which result from their analytical expressions: below a value of around 50 m.r.d.^{2}, S is varying much more than F^2, this latter being less efficient in revealing the texture strength. The reverse is true above 50 m.r.d.^{2}.

More work is needed in the same direction, in order to comprehend the effect of the number of pole figures in the OD refinement by the WIMV approach. Also, the crystal symmetry and the orientation of the component(s) influences should have to be elucidated.

3. Texture to Physical Properties Correlation

As a consequence of more and more sophisticated elaboration techniques, samples are often in a microstructural state which is textured, i.e. between a perfect single crystal (for which we, generally, know the microscopic physical tensors) and a perfect powder (which does not exhibit any anisotropy). "In between" means also that we do not know quantitatively how the texture influences the resulting macroscopic properties. As we mentioned it already, a tremendous effort has been put over years for the prediction of mechanical properties, and we will not discuss this here. The geometric mean formalism [Matthies et Humbert 1995] for instance allows the simulation of elastic stiffnesses of single phase materials within a reasonable degree.

In our case we focused on the correlation that exist between texture and other physical properties, generally linked to technological developments. Unfortunately, for most of them there is no working theory to simulate the macroscopic tensors. For some properties like superconducting current densities, the mean approach is just not valid, because these properties are not additive. In such cases we show, however, that we can bring light on the texture influence. In the case of magnetic properties, we show that some formalism can be elaborated, which can help simulating magnetisation curves of easy-axis or easy-plane materials, provided the texture is known.

3.1. Critical current densities (Jc) in thin films of Y-Ba-Cu-O

(main collaborator: M. Pernet, LC-CNRS, Grenoble, France)

This was the starting point of our studies, beginning back in 1992. We will not go thoroughly in the details which have been published but only present a short report (next paper) which shows how strong can be the texture effects in such compounds. Some percents of several kinds of misorientations were found to result in a dramatic decrease of Jc. This was not expected from the original works on orientation dependence of Jc [Dimos et al. 1988; Dimos, Chaudhari et Mannhart 1990]. However they isolated individual grain boundaries which is considerably different from real samples with distributions of grains, then boundaries. More details can be found elsewhere [Chateigner 1994].

3.2. Critical current densities of mono- and multifilament tapes and wires in the (Bi,Pb)-Sr-Ca-Cu-O system

(Main collaborator: H.-R. Wenk, DGGB, Berkeley-CA, USA)

In these compounds the relatively low critical current densities are also partly due to the misorientations of crystals [Kawasaki et al. 1993], and the filament-like shape of the samples makes them not possible to quantitatively analyse their texture with x-rays, because of their irregular geometry. Many reports mention larger critical current densities in multifilaments than in monofilament tapes, than in wires [Jin et Graebner 1991]. The multifilament technology have been chosen by CEA for superconducting cables [CEA technologie 2000]. It was also reported [Grasso et al. 1995] that the critical current densities was varying along the width of the monofilaments, giving rise to larger current carrying capabilities on the edges. Using a micrometer beam at ESRF, we were not able to see any texture variation along the width of the tapes (not published), indicating that another effect should be involved.

Using neutron diffraction we were able to measure the textures of multi- and mono-filament tapes and wires of the "2212" and "2223" phases of the Bi,Pb-Sr-Ca-Cu-O system. The results are coherent with the respective critical current densities measured in such systems. Particularly, using the texture results, one can explain easily the relatively poor current carrying efficiencies of the rolled wires and unidirectionally pressed powders.

3.3. Anionic conductivity in the Bi-Co-V-O system

(Main collaborator: P. de Rango, LC-CNRS, Grenoble, France)

One of the challenges in the elaboration of superionic conductors for batteries is to remove grain boundaries that perturb current flowing and to optimise anisotropy. We used texturing methods previously developed for superconductors in order to elaborate ceramics of the $(Bi,Co)_4V_2O_{11-\delta}$ compound. Inducing the texture removed most of the grain boundary effects (the ones that are seen with impedance spectroscopy) and allowed to obtain exploitable conductions. This work shows which texture level is necessary to obtain reasonable anionic conductivity in this material, by there avoiding the always difficult problem of the single crystal elaboration.

3.4. Remanent polarisation and pyroelectric coefficients in PTL and PTC films

(Main collaborator: J. Ricote, DMF-CSIC, Madrid, España)

$Pb(La/Ti)O_3$ (PTL) and $Pb(Ca/Ti)O_3$ (PTC) perovskite-related systems exhibit relatively high pyro and ferroelectric properties which make them potential sensors and acoustic waves devices, to be integrated. In the tetragonal form the polarisation vector lies along the **c** axis of the structure, which should ideally be aligned with the normal of the films in order to benefit of optimised properties. In the view of integrated devices, only silicon single crystals appear reasonable as substrates because of their cheapness and extended availability. Hence, some anti-diffusion barriers have to be deposited between the film and the substrate (generally TiO_2), on top of which is placed a Pt electrode used later to induce perpendicular polarisation. All these layers result in complex diffraction diagrams (Figure 11), with a lot of overlapped peaks. Some of the peaks from the ferroelectric film are hopefully enough separated from the other phases and can be used for QTA.

At this stage a difficult question arises: how much can we dissociate 90° and 180° grain or domain wall boundaries ?

The 90° boundaries are provided by the two types of orientation components detected in such films: either with **a** or **c** axes perpendicular to the film plane, the first one giving no perpendicular contribution to the net polarisation of the film. Since the tetragonal structure comes from a slight distortion or rotations of oxygen octahedra in the perovskite structure, it results in a pseudo-cubic structure. This structure exhibits only strongly overlapped diffracted peaks. For instance, the 001 and 100 lines are not separated by more than 0.2° in 2theta. It appeared that the direct integration methodology, using overlapping deconvolution at the OD refinement step, was able to provide results coherent with the measured properties (next papers). This analysis will have to be completed with the structure/texture pattern methodology, the peak fit procedure having cancelled because of too much close lines.

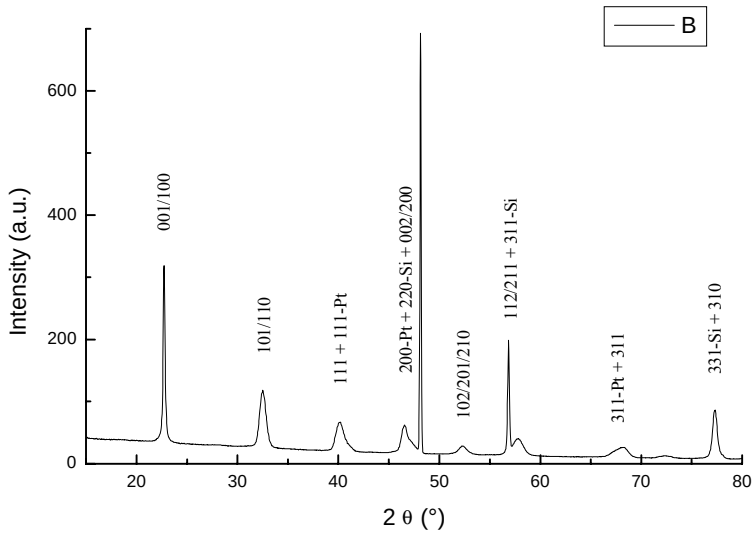

Figure 11: Sum diagram of a PTL film showing the diffraction lines of the component layers

The correlation between textures and physical properties in ferroelectric thin films is understandable on the base of the crystal tensors, that have to be somehow averaged on the distribution of orientations. It is not clear at the moment if piezo or ferroelectric properties can be directly averaged. This will have to be consistent with experimentally measured values. However, the first step towards a simulation of the macroscopic properties is to understand how one can handle the elementary single crystal tensors.

Figure 12 shows the single crystal dielectric constant of PZT in the g=(0,0,0) orientation, normalised to the largest value. This plot illustrates that the c perpendicular orientation favours large properties, but not the maximum ones, located around the {102} normals. Calculations are based on the bulk values of the PZT single crystal, and on a recently developed formalism which can deal with any tensor order, even asymmetric [Du, Belegundu et Uchino 1997]. Our programs which will be updated in the future for other orientations and orientation distributions.

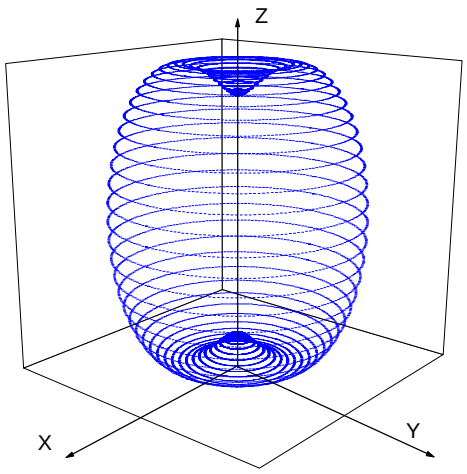

Figure 12: Dielectric constant tensor for a single crystal of the tetragonal PZT phase in the g=(0,0,0) orientation.

The 180° domain walls are not measurable using normal diffraction because of the Friedel's law. Hopefully, the polarisation process in principle provides a full reorientation of the domains. However, we tried to use anomalous scattering at ESRF on $Pb(Zr/Ti)O_3$ (PZT) films. The main goal of this experiment was to see if we could detect enough signal difference before and after the Zr absorption edge, that could provide a full QTA analysis. The difference we could measure in the scattered intensities was very small and one has perhaps first to find larger anomalous signals.

3.5. Magnetic properties of easy-axis and easy-plane magnetisation compounds

In order to optimise macroscopic magnetic properties, a lot of efforts have been addressed to the development of texturing processes [Legrand 1996, Liesert 1998, Rivoirard et al. 2000]. In easy-axis materials, the ability for the magnetic moments to be aligned along one specific crystallographic axis is of fundamental importance for hard magnetic properties. Then, many works focus on the characterisation of the anisotropic behaviour like magnetisation curves in intermetallic compounds [Searle et al. 1982, Qun et al. 1992, Elk et Hermann 1993, Yan et al. 2000]. These works generally concentrate on the estimation of the crystallite distribution from the magnetisation curves, using differently defined orientation or misalignment parameters. However such orientation distribution factors are accessible for any crystalline materials using diffraction measurements and QTA. Since many parameters influence the magnetisation curves, it is important to independently measure them as much as

possible. We chose in the first paper to illustrate how are correlated the anisotropic magnetisation curves with the texture in the Sm-Co easy-axis system. Then, we propose a methodology for the simulation of magnetic anisotropic properties of the easy-plane oriented ferrimagnetic $ErMn_4Fe_8C$ carbide.

3.5.1. Easy-axis magnetisation of the Sm-Co compounds (Main collaborator: B. Legrand, EPM-MATFORMAG, Grenoble, France)

Paper

3.5.2. Easy-plane magnetisation of $ErMn_4Fe_8C$ (Main collaborator: M. Morales, LC-CNRS, Grenoble, France)

Intermetallic compounds of rare-earth elements (R) and 3d transition metals (M) having the structure type $ThMn_{12}$ are characterised by the existence of interstitial sites suited for the incorporation of the H, C or N light elements. Due to the insertion of these light elements, most of the fundamental magnetic characteristics like 3d magnetisation, Curie temperature and magneto-crystalline anisotropy are modified [Soubeyroux et al. 1995]. Previous studies on the insertion of H and C atoms in the $ErMn_{12-x}Fe_x$ compounds ($x \leq 9$) have pointed out the important role played by these interstitial atoms for their fundamental properties with the transformation of a weak to a strong ferromagnetism [Morales et al. 2001a]. The starting compound $ErMn_4Fe_8C$ was prepared by induction melting of the metal constituents, then carburated, and exhibits a Curie temperature of 450 K [Morales et al. 1999]. In order to determine the easy macroscopic direction of the magnetisation (EMD) and to measure the magnetic anisotropy, two differently aligned samples were prepared by solidification of a resin-powder mixture under an applied magnetic field, H_{text}, of 0.5 T. Both samples were 4 mm diameter and 5 mm long cylinders. Sample A was solidified with $\mathbf{H}_{text}$ applied parallel to the **z** axis of the cylinder (Figure 13a), while Sample B, was rotated (10 rd/mn) around its **z** axis, with $\mathbf{H}_{text}$ applied perpendicular to it (Figure 13b). QTA was performed on Sample B using the LPEC dispositive. Magnetisation measurements were carried out using an extraction magnetometer on the oriented powders with an applied magnetic field, $\mathbf{H}_{meas}$, parallel and perpendicular to $\mathbf{H}_{text}$ (Figure 14) for Sample A and B respectively. Neutron diffraction experiments on the $ErMn_4Fe_8C$ free powder were performed at T = 280K using the D1B diffractometer (λ = 2.522Å) in order to determine the microscopic magnetic properties.

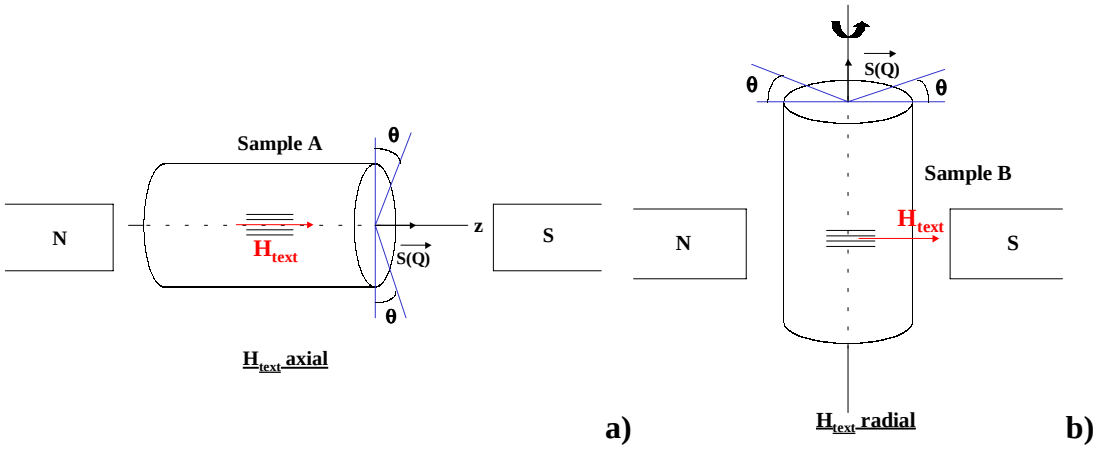

Figure 13: Classical (**a**) and Rotation (**b**) alignment procedures. The diffraction measurement geometry is also shown.

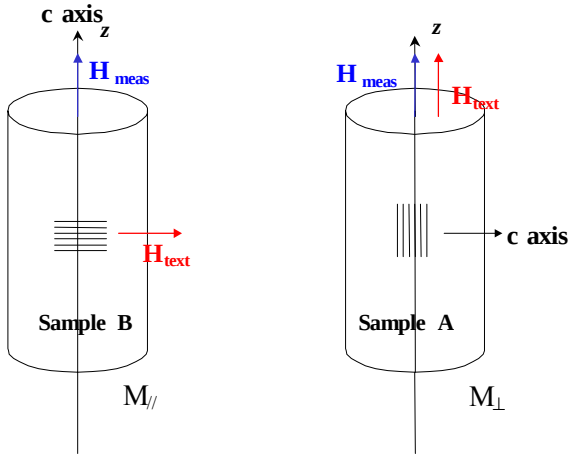

Figure 14: Configurations for the magnetisation measurements: $M_{//}$ corresponds to the magnetisation curve of Sample B, with $\mathbf{H}_{meas}$ // **c**, and $M_{\perp}$ to the $\mathbf{H}_{meas} \perp$ **c** configuration (Sample A).

The x-ray diffraction diagrams measured with the scattering vector parallel and perpendicular to $\mathbf{H}_{text}$ (Sample A and B respectively) exhibit different {220}/{002} intensity ratios, with favoured {220} reflections when $\mathbf{H}_{text}$ is applied parallel to **z** (Sample A), and favoured {002} lines for $\mathbf{H}_{text}$ perpendicular to **z**. This indicates that the mean EMD is located in the basal plane of the structure. QTA was performed on the oriented carbide with $\mathbf{H}_{text}$ perpendicular to **z** (Sample B). The pole figures are representative of a fibre texture, with crystalline axes randomly distributed around their normal (**z** axis). The {001} planes are in a major fashion aligned perpendicularly to the cylinder **z** axis with a maximum orientation density about 3.9 m.r.d.. The entropy S of the distribution is equal to –0.13, synonymous of a weak texture, but which would be sufficient to induce an anisotropy of the magnetic behaviour.

The anisotropy field, H_A, is calculated from the magnetisation curves and will be used in their simulations.

Numerical simulation of the M(H) curves

The magnetisation M(H) in an applied magnetic field H_{meas} can be expressed by:

$$M(H_{meas}) = M_S \cos(\theta_0 - \theta) \qquad (10)$$

where M_S is the saturation magnetisation, θ is the angle between the **c** axis of the crystals and the magnetisation direction, and θ_0 the angle between $\mathbf{H}_{meas}$ and the **c** axes of the crystallites (Figure 15).

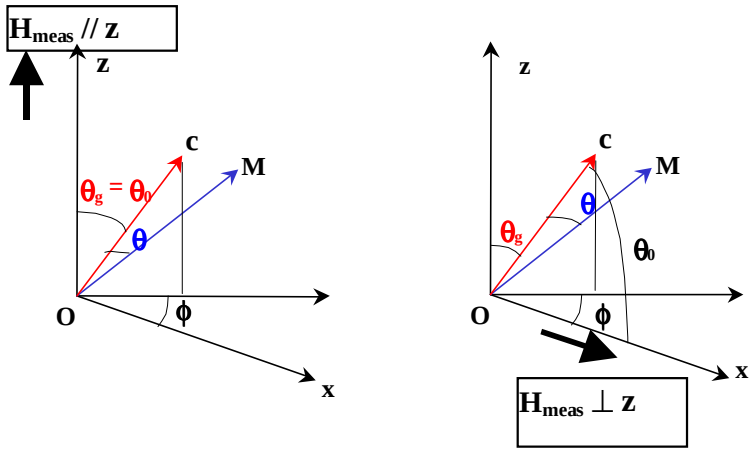

Figure 15: The two possible configurations for the measurement of the magnetisation curves. We use the left one in this work.

The energy of a sample in an applied magnetic field can be expressed in a first approximation by:

$$E(H_{meas}) = K_1 \sin^2\theta - H.M_S \cos(\theta_0 - \theta) \qquad (11)$$

where K_1 is the anisotropy constant. In this equation, the first term represents the anisotropy energy and the second the Zeeman energy. Under the equilibrium condition we have:

$$\frac{dE}{d\theta} = 0 \qquad (12)$$

which gives from (10):

$$H_{meas} = \frac{2K_1 \sin\theta \cos\theta}{M_S \sin(\theta_0 - \theta)} \qquad (13).$$

With an anisotropy field $H_A = 2K_1/M_S$, the equilibrium condition becomes:

$$\frac{H_{meas}}{H_A} = \frac{\sin\theta \cos\theta}{\sin(\theta_0 - \theta)} \qquad (14)$$

As the $ErMn_4Fe_8C$ compound magnetisation curves are not saturated for a H_{meas} of 10T, we use for the evaluation of the saturation magnetisation M_S a polynomial extrapolation method. We consider that the magnetisation follows a saturation law established experimentally for strong magnetic fields. Thus, at strong applied fields there is no more domain wall displacement and the global magnetisation variation is only due to the rotation of the magnetic moments:

$$\frac{M}{H} = \chi_0 - \frac{M_s}{H} - \frac{AM_s}{H^2} - \frac{BM_s}{H^3} \qquad (15)$$

where χ_0 is the initial magnetic susceptibility and A, B, are coefficients to determine. The fit of $M_{//}/H=f(1/H)$ curve at T = 280K gives $M_S = 5.24\ \mu_B$/fu.

The studied sample can be represented by crystallites which have their crystallographic **c** axes distributed uniformly around a texturation direction, the **z** axis (Figure 15). The angular distribution of the magnetic moments, linked to the basal planes of the tetragonal structure, can be described by the probability function $F(\theta_g, \varphi)$ of finding the **c** axis in a direction given by the θ_g and φ angles (Figure 15). The θ_g angle measures the deviation of the **c** axes from the **z** axis (it is equivalent to the polar angle of the pole figures), and φ gives the location of the projection of c in the (x,y) plane (the azimuth of the pole figures). We will see now that the probability function is strongly correlated to the pole figures as measured by diffraction. For magnetic moments, we should apply the normalisation condition [Searle et al. 1982]:

$$\int_{\theta_g=0}^{\frac{\pi}{2}} \int_{\varphi=0}^{2\pi} F(\theta_g, \varphi) \sin\theta_g \, d\theta_g \, d\varphi = 1 \qquad (16)$$

For a random distribution (isotropic sample), $F(\theta_g,\varphi)$ is a constant equal to 1. For a textured sample, it is a distribution that has to respect in some measure the crystallite distribution function, if the magnetic moments are linked to crystallography, which has been proved for the $ErMn_{12-x}Fe_xC$ compounds [Morales et al. 2001b].

In our case, $\mathbf{H}_{meas}$ is parallel to the texturation direction **z**, perpendicular to the mean direction of the EMD. It then comes that $\theta_g = \theta_0$ and the component of the magnetisation along **z** is given by:

$$\frac{M_{//}}{M_S} = 2\pi \int_0^{\frac{\pi}{2}} G(\theta_g) \sin\theta_g \cos(\theta_g - \theta)\, d\theta_g \qquad (17)$$

where θ is calculated with the equation (14) for every value of H_{meas} and θ_g, the 2π factor comes from the integration of the $F(\theta_g,\varphi)$ function over φ for this axially symmetric texture, and $G(\theta_g)$ is the radial evolution of the distribution of the textured volume.

The texture experiments allow the measurements of the radial {001} pole profile, $G(\theta_g)$. We obtain a best fit with a Pseudo-Voigt (PV) shape function with a Half-Width at Half Maximum (HWHM) of 12.2° and a randomly distributed part of the volume, ρ_0 = 0.5 m.r.d. (minimum of the distribution). From the definition of the pole figures, ρ_0 is directly the random volumic ratio.

Then, the contribution of the random part to the magnetisation is the classical random magnetic signal M_{random}, obtained on the free powder, times the volume ratio associated to this random component.

The contribution to the magnetisation of the textured part can be written:

$$G(\theta_g) = (1 - \rho_0) PV(\theta_g) \qquad (18)$$

The Equation (17) then becomes:

$$\frac{M_{//}}{M_S} = 2\pi \int_0^{\frac{\pi}{2}} (1 - \rho_0) PV(\theta_g) \sin\theta_g \cos(\theta_g - \theta)\, d\theta_g + \rho_0 M_{random} \qquad (20)$$

$$\frac{M_{//}}{M_S} = 0.5 M_{random} + 0.5 * 2\pi \int_0^{\frac{\pi}{2}} PV(\theta_g) \sin\theta_g \cos(\theta_g - \theta)\, d\theta_g \qquad (21)$$

With this formalism, we have simulated the experimental magnetic curves $M_{//}/M_S$ for the low values of the H_{meas}/H_A ratio ($H_{meas}/H_A < 2$). Indeed, for higher applied magnetic field this model does not take into account the rotation of the various magnetic moments which are in the basal plane and have progressively to be aligned with the direction of the applied magnetic field. The best agreement between the calculated and the observed $M_{//}/M_S$ curves is shown in Figure 16.

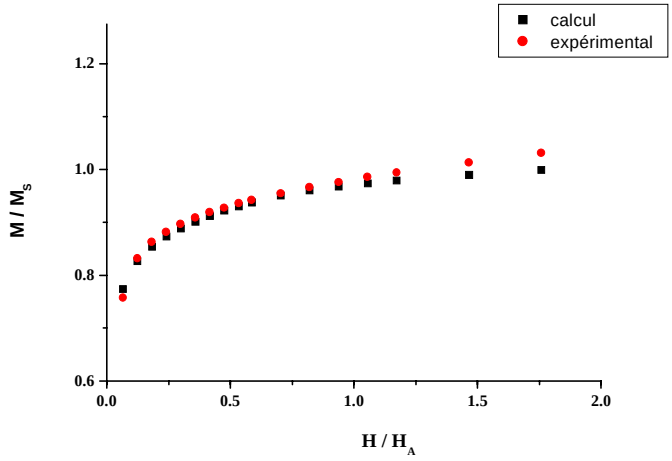

Figure 16: $M_{//}$ measured and simulated anisotropic magnetisation curves of our magnetically aligned carbide

Paper

3.6. Levitation forces in bulk melt textured Y-Ba-Cu-O
(Main collaborator: X. Chaud, CRETA-CNRS, Grenoble, France)

This work is aiming to clarify which of the main parameters of the Y-Ba-Cu-O melt-textured compounds act beneficially on the texture and if there is a correlation between this texture and the levitation forces. A lot of different texturation processes have been developed in order to enhance superconducting properties in bulk materials [Jin et Graebner 1991]. We chose here to concentrate on three distinct parameters: the Sm-Ba-Cu-O seed, the thermal radial gradient and the high magnetic field effects. Similarly as previously for thin films (see § 3.1.), people have concentrated their interests on individuals and described the effect of the orientation for this individual on the wanted property [Shi et al. 1997], considering it as a single domain. None have tried to analyse the effect of a distribution of domains as we propose here.

We can perhaps see in a more evident way the effect of the texture discussed in the preceding paper. On Figure 17, we present the levitation force variation versus the texture entropy. With the exception of one point, which one can discuss from the point of view of the paragraph 2, the entropy is a fairly good factor to correlate with the wanted properties.

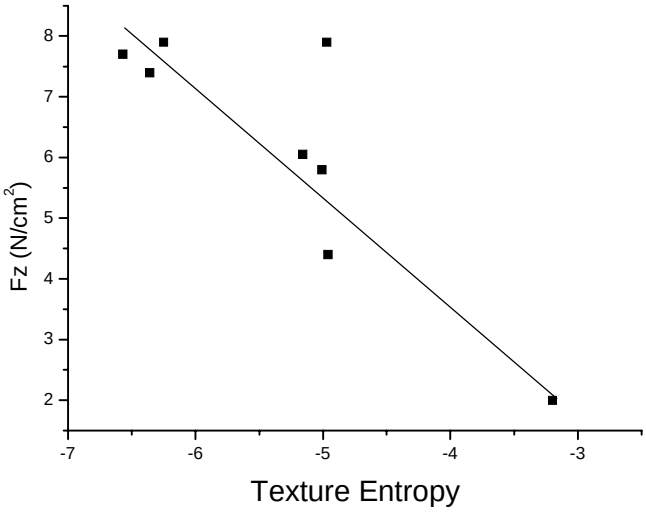

Figure 17: Levitation force to texture strength correlation in melt textured samples of Y-Ba-Cu-O

4. Texture effect on techniques of analysis

The effect of the preferred orientations on characterisation methods has been of interests for instance in ESR [Pellerin et al. 1994] and Mössbauer [Grenèche 1981, Grenèche et Varret 1982] spectroscopies. However, if the theoretical developments were thoroughly detailed, the quantitative dispersion of crystallites has never been quantitatively measured and taken into account in the analysis, as done in the previous paragraph. We present here two examples for which it became recently possible.

4.1. Polarised EXAFS spectroscopy

(Main collaborator: A. Manceau, LGIT-IRIGM, Grenoble, France)

These works concern self-supporting films of nontronites, hectorites and montmorillonites. The initial idea was to simplify the EXAFS spectra using strongly textured samples and polarised radiation. It proved to be interesting not only to "clean-up" the spectra but, because of cleaner spectra, to enlarge the available range of the reciprocal space hereby providing more details in the structural analysis. This structural information is of much interests since it provides local ions positions at relatively long distances from the probed ion (where EXAFS oscillations strongly overlap), which is particularly important to characterise if someone wants to know the ion take-up efficiency, like in polluted phyllosilicated soils.

This structural information would be provided in principle by diffraction experiments. However, the large turbostratic character of the concerned samples makes such experiments very hard to practice, because of the lack of coherence for in-plane and oblique scattering lines. A formalism has been developed by Drits et Tchoubar (1990) for perfectly turbostratic materials, in which oblique rays are dealt identically as in-plane ones. This formalism is perfectly adequate for powders where diffracted signals are averaged and put close to background. However for strongly textured samples, we detected some diffraction lines possibly provided by oblique rays (see the following papers). These were used in the OD analysis and fit well with it. They could have come from impurities (we try to work on close-to-real samples), but they are more or less systematic with the crystal structure. Furthermore, they are decreasing with decreasing texture strengths. We also tried to reproduce the powder diffraction patterns with a loose of the scattering coherence like with the Le Bail approach [Le Bail 1995], without success. This is actually an open problem and it would be really interesting to test a combination of the two approaches (Drits + Le Bail).

4.2. Diffraction combined analysis

(Main collaborator: L. Lutterotti, DIM, Trento, Italy)

Introduced some years ago as the RTA method [Lutterotti et al. 1997] using the WIMV algorithm, this kind of analysis is crucial for non-destructible samples of unknown or roughly known structure, texture or microstructure in general. It has also been more recently developed using the generalised spherical harmonic formalism with [Wang et al. 1997] or without [Von Dreele 1997] a maximum texture-entropy assumption. The general idea is: if we do not know exactly the structure we cannot solve the texture and vice-versa, and this is true for any of the parameters which are visible in scattering diagrams. For instance, if we do not know the real thickness of a film, how to properly correct for it in the texture patterns ? Then we have to combine reflectivity and texture analysis (see ESQUI project)...

We give an example in the following paper of a multiphase sample analysis with different particle sizes and texture for the two phases. In this case we were interested in quantitatively determine the texture, the phase volumic ratio, the crystallite sizes and the microstrains of the two phases. The experiments were operated at the D20-ILL beamline. The microstrains were revealed to be negligible.

5. QTA of mollusc shells

The growth of mollusc shells (monoplacophoras, cephalopods, bivalves and gastropods) is strongly influenced by animal proteins [Weiner et Traub 1980, Weiner et Traub 1981, Falini et al. 1996]. This influence is expressed in the crystallographic texture, as we could observe it studying more than 60 different layers of many species. The shells are constituted of several layers, crystallising in the aragonite (Pnma space group) or calcite (R-3c) system, which texture varies in strength and quality.

5.1. Aragonitic layers

(Main collaborator: C. Hedegaard, IB-DEG, Aarhus, Denmark)

The diversity of the texture patterns runs from the complete absence of texture to extreme texture strengths, via orientation complexities and intermediate strengths. Textures are similar for closely related species et differ for more distant species. The more surprising is that commonly accepted growth schemes, with main crystal axes aligned with main shell axes, were found to be unacceptable. Also, the SEM and texture analyses were employed and showed to provide different views of the same entities, proving that QTA can bring non-redundant new insights for phylogenetic discussions.

The following papers deal with aragonitic layers.

Paper1 Paper2 Paper3

From these studies it would be still too much ambitious to draw out quantitative character analyses. We only have studied few tens of layers, which is nothing compared to the diversity of molluscs. However, a first estimate of the importance of the texture analysis can be illustrated looking at the nacre layers of the major clades. Nacre is believed as the ancestral mineralisation type in molluscs. Figure 18a shows the actual phylogeny of molluscs as deduced from the most recent works of Ponder and Lindberg (1997) for gastropods, Waller (1998) and Bowman (1989) for bivalves. In black on this figure are the nacred species. Using this tree we see a lot of events where nacre was abandoned.

Figure 18b is a reconstruction of the tree of Figure 18a, which includes some of the texture data: **a** and **c** axes patterns. We wish to investigate the homology of texture patterns and code each texture as a binary character (present or absent), map the characters on our phylogenetic hypothesis (figure 18a), and evaluate the character distribution with the program PAUP under the ACCTRAN and DELTRAN assumptions, favouring reversals and parallelisms, respectively, in an equally parsimonious setting (Swofford and Begle, 1993). One can see clearly that much less events are necessary in this tree than in the previous one. Furthermore, each of the dissociated nacres show typical texture patterns. For instance, gastropods exhibit fibre textured nacre while cephalopods and bivalve's nacre is double twinned with 50% and lower percentage of twinned volume, respectively.

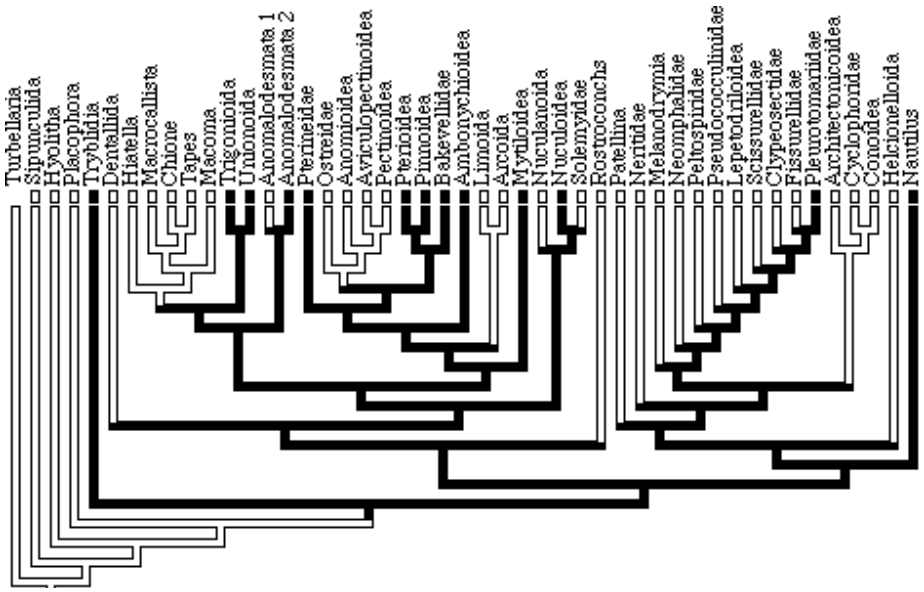

a)

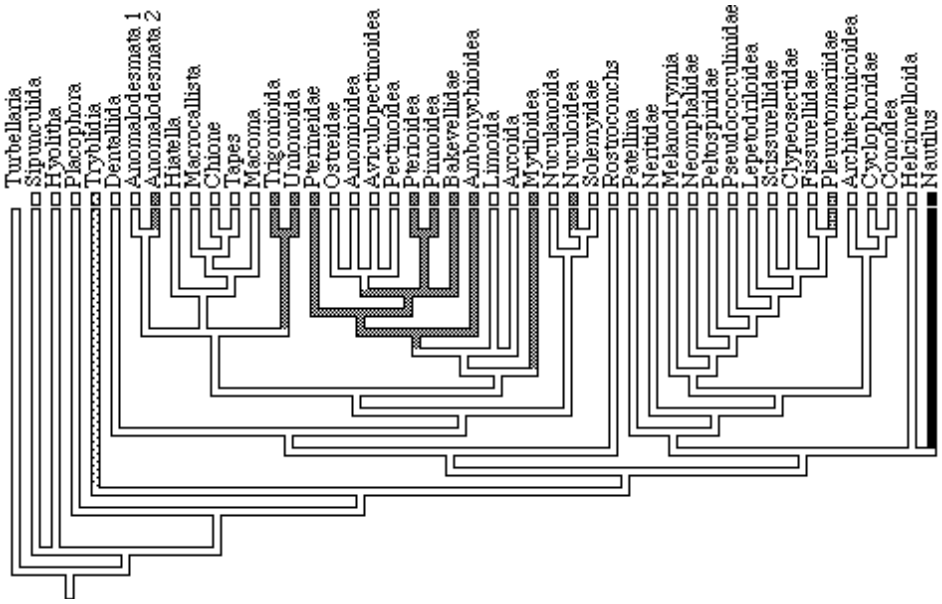

b)

Figure 18: a): Actual phylogeny of mollusc from literature. **b):** reconstructed phylogeny including some texture data. In black or shaded are the nacre-containing species.

5.2. Calcitic layers

(Main collaborator: L. Harper, DESC, Cambridge, UK)

There is good evidence to suggest that the earliest bivalves were all entirely aragonitic and of rather simple construction from two microstructural types. However, later, bivalves evolved a further 5 microstructural types (2 of them calcitic) and utilised these in a variety of different arrangements. The result is that the bivalve microstructure and mineralogy is extremely diverse across the class and is, therefore, thought to be a valuable character for phylogenetic analysis.

Two major types of calcite microstructure are identified: prisms, which usually occur on the outside of the valve, and foliae which tends to occupy the bulk of a shell (e.g. oysters: *C. gigas*). Of these, calcite prisms are perhaps the most interesting because there is good evidence that calcitic prisms have evolved at least four times independently within the Bivalvia, in the mussels, pterioids, chamids and the extinct rudists.

The data presented here is from the calcitic prismatic layer of bivalves from members of the sub-class Pteriomorphia. This broad group encompasses two of the calcite secreting clades, the mussels and the pterioids. It is therefore, of great value to compare the form of the calcite

crystals within members of these taxa. *B. thermophilus* and *M. edulis* are both mussels, the former being an important component of deep sea vent faunas. Although both have calcitic outer shell layers it is clear from texture analysis (Table 2) that the two are separate innovations of the calcitic shell layer, with different alignment schemes of their **a** axes.

	Layer type	ODF Max (mrd)	ODF min (mrd)	RP0 (%)	RP1 (%)	c-axis	a-axis	{001} Max (mrd)	F^2 (mrd^2)	- S
Pinna nobilis	OP	303	0	50	29	// N	random	68	29	2.3
Pteria penguin	OP	84	0	29	15	// N	random	31	13	1.9
Amussium parpiraceum	OP	330	0	53	33	// G	<110> // M	20	31	2.6
Bathymodiolus thermophilus	OP	63	0	25	18	// G	// M	27	13	1.9
Mytilus edulis	OP	207	0	41	25	75° from N	<110> // M	23	21	2.2
Trichites	P	390	0	52	28	15° from N	random	56	41	2.2
Crassostrea gigas	IF	908	0	45	31	35° from N	// M	>100	329	5.1

Table 2: Texture analysis results for the calcitic layers of seven species.
OP: Outer Prismatic, IF: Inner Foliated layers

The pterioids are represented by *P. nobilis*, *P. penguin*., *Trichites sp.*, and *A. papiraceum*. Although these ostensibly all belong to the same clade of calcite secretors it is important to establish the degree of similarity or difference between the various taxa.

In particular, recent molecular schemes have placed the pteriids (i.e. *P. penguin*) as a sister-group to the pinnoids (*Pinna* and possibly *Trichites*). All three species exhibit similar textures, but *Trichites*, if we except its slightly inclined **c** axis distribution, shows an ODF maximum closer to the pinnoids than to the pteriids.

A. parpiraceum belongs to the superfamily Pectinoidea which, according to some phylogenetic schemes at least, is further removed from the pteriids and pinnoids, than are the mussels. If this is so, then calcite secretion in the pterioid group may be polyphyletic and thus we might expect the Amussium to display different textures to both the Pinna + Pteria and the mussels. This is actually what we have measured as textures in Amussium, which presents a clearly not random alignment of its **a** axes (i.e. is different of *Trichites*, Pterids and Pinnoids), a **c** axis distribution in the plane of the shell (not like *M. edulis*) and <110> directions aligned with **M** (where *B. thermophilus* has its **a** axes).

As a conclusion of this paragraph, we should mention that *Trichites* are fossilised species. Another aim of this study is also to find if fossil taxa have or not conserved their textures, and if we can correlate them to actual living species.

6. QTA approach of polymers

(Main collaborator: F. Poncin-Epaillard, LPCI, Le Mans, France)

In paragraph 1.3. we mentioned the textural analysis of polypropylene plasma treated films. Non treated films are fully amorphous and no QTA is made possible. But after 10 min of plasma irradiation, the scattering diagram is the one of Figure 2, which allows a QTA from the peak profiles. Figure 19 shows the peak variation with the tilt angle of the goniometer. The texture developed in such films is not strong (F^2 = 1.2 m.r.d.^{2}) but significant. Also there is no appreciable difference after 12 min of treatment. The inverse pole figure calculated for the normal of the film (Figure 20) shows this texture. It indicates that the **c** axes of the structure align in the plane of the film, but without preferred alignment in the film plane (planar texture). To our knowledge it is the first QTA documented for such compounds.

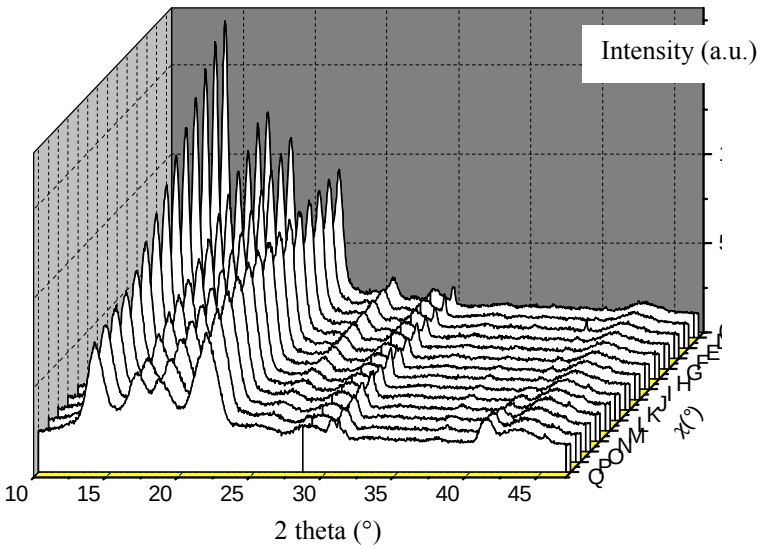

Figure 19: Variation of the polypropylene peaks with the tilt angle of the goniometer, indicating a texture stabilisation during the plasma treatment

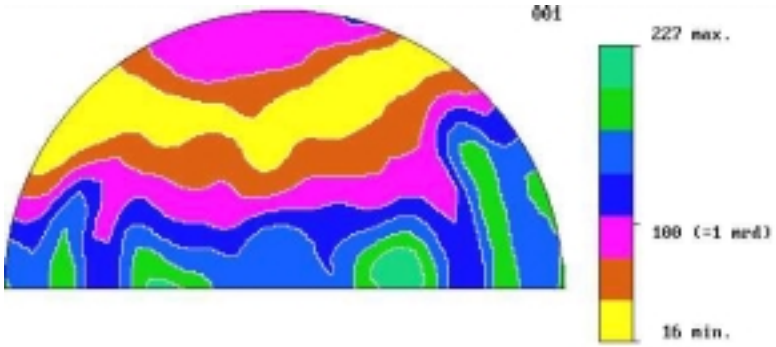

Figure 20: Inverse pole figure for the normal of the film plane. All normals from <100>* to <010>* are more or less equally present along the film normal. Linear density scale, equal area projection.

7. Conclusions and Perspectives

We have shown a global overview of the importance of texture analysis for optimising macroscopic anisotropic properties, controlling growth of materials, simulating some physical properties, explaining and extending anisotropic signals and in providing new insights in mollusc shell description. All these works and efforts will be continued. In the near future we will furthermore concentrate on two experimental novelties, which are lastly described in the two next paragraphs.

7.1. New optics of the goniometer

We recently designed a new system for the x-ray optics of the goniometer, making use of the mechanical facilities of the DESC. The main interest lies in the possibility to exchange both monochromator and radiation easily, means without loss of the goniometer centre. Indeed, it is very difficult to work with the PSD on fluorescent samples, since it is impossible to place a back monochromator. Also, working with several wavelengths can provide different independent views of the same system. Figure 21 shows a view of the new system which allows the necessarily concentric rotation of the three axes (radiation source, monochromator, x-ray line).

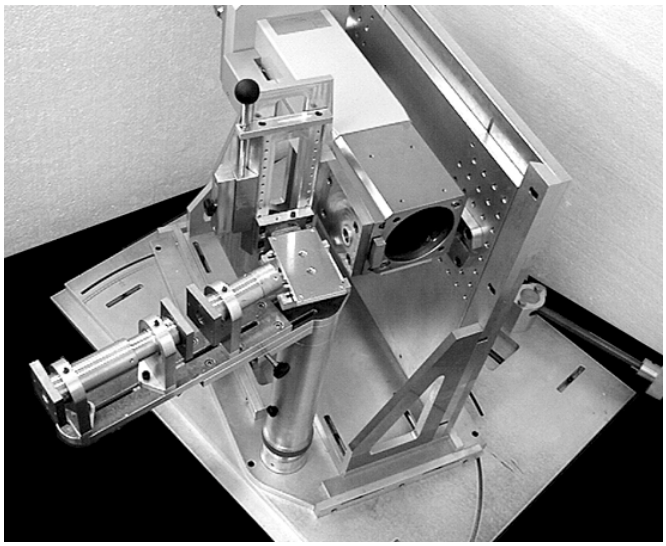

Figure 21: View of the new optic system (monochromator housing removed)

7.2. Laüe orientation mapping

The EBSD method as developed on the SEM allows the full determination of the OD and of the misorientation distribution function [Wright et Adams 1992, Wright 1993]. However, to speak only about its disadvantages, the techniques is limited by the crystalline state of the samples, and concerns the very near surface. Figure 22 compares results obtained with x-rays with the ones obtained with EBSD on *C. gigas*, one of the best shell candidates to analyse with EBSD, because of its relatively flat geometry.

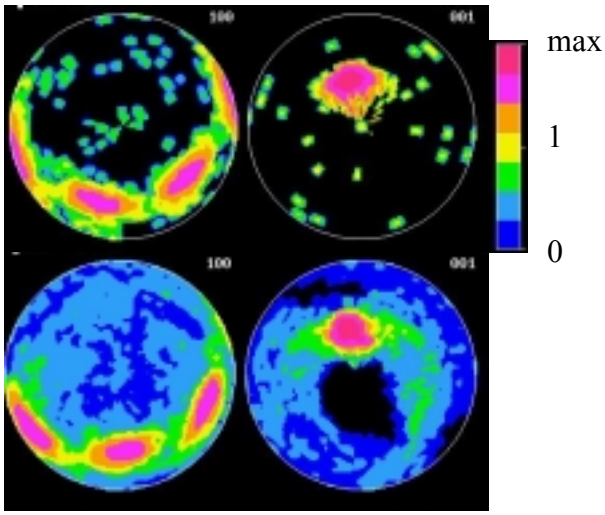

Figure 22: {100} and {001} pole figures of *Crassostrea gigas*, obtained from EBSD (top row) and x-ray (bottom) analyses. Max = 100 m.r.d. Logarithmic density scale, equal area projections.

Approximately 70% of the 2600 Kikuchi patterns were not satisfactorily indexed in the EBSD experiment, resulting in a quite poor definition of the low density levels. We suspect in this example that small grains are not indexed with EBSD, while the x-ray profile includes them.

An alternative has been worked out at synchrotron beamlines in the transmission Laüe geometry [Wenk et al. 1997]. Even if very small grains will always be measurable with difficulty, this alternative would have to be pursued, why not with classical generators, though for large grains. For instance when using an electron beam is not possible like in ice samples.

7.3. ESQUI project

This project will finish on february 2003. It concerns the determination of structure, texture, strain/stresses, thickness, ... for microelectronic films and devices. For instance, one

of the actual problems we meet is such a determination in La-Li-Ta-O thin compounds, in order to understand which microstructural parameters are dominating the ionic conductivities. The less textured films (Figure 23) are already so much oriented that a 5°x5° measurement grid does not provide reliable OD refinement with the usual WIMV program. We know that at least four orientation components can be stabilised, and (from raman spectroscopy experiments) that residual stresses are present in the film. Furthermore, the film composition influences the peak positions...

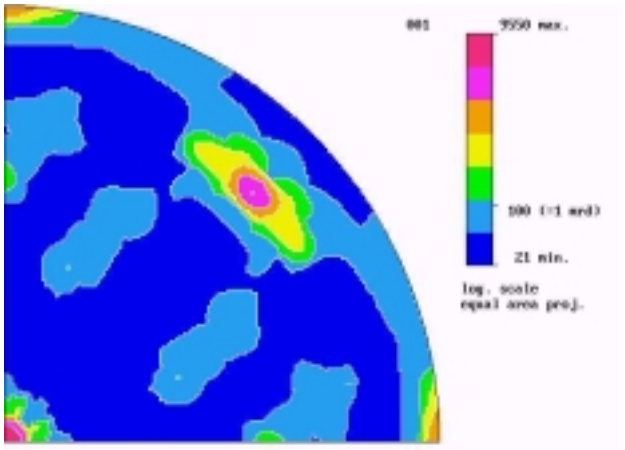

Figure 23: Inverse pole figure of a perovskite-related tetragonal $Li_{3x}La_{2/3-x}Ti\square_{1/3-x}O_{3-\delta}$ film for the normal to the film plane.

We hope the project's main achievements will make available:

- The production of standard samples with gradual x-ray analysis difficulties
- The optimisation of the G-space using the CPS, as developed in MIMA (BEARTEX)
- The incorporation of more resoluted measurement grids
- The combined texture/structure analysis using the CPS
- The incorporation of the residual stresses analysis
- The combination of these with a Fresnel-based algorithm for specular x-ray reflectivity data
- The determination of the Electron Density Profile from specular reflectivity data.

All these novelties are planned to be incorporated inside the already existing MAUD package [Lutterotti et al. 1999].

References

Bowman B.H. (1989). *Non-Clocklike Evolution in the Ribosomal RNAs of Bivalve Molluscs*. Ph.D. Dissertation, University of California at Berkeley, 245 pp.

Bunge H.-J. (1982). 'Texture Analysis in Materials Science', (P.R. Morris Trans.) Butterworths, London.

Bunge H.-J. & Esling C. (1982). "Quantitative Texture Analysis", Bunge and Esling Ed., DGM, Germany.

Bunge H.-J., Wenk H.R. & Pannetier J. (1982). Neutron diffraction texture analysis using a 2θ position sensitive detector. *Textures and Microstructures* **5** 153-170.

Chateigner D. (1994). Thesis (Université J. Fourier, Grenoble-France). Texture cristallographique de céramiques et de couches minces supraconductrices $Yba_2Cu_3O_{7-\delta}$ en relation avec les propriétés physiques.

Chateigner D., Wenk H.-R., Patel A., Todd M., Barber D.J. (1997). Analysis of preferential orientations in PST and PZT thin films on various substrates. *Integrated Ferroelectrics* **19**, 121-140.

Chateigner D., Wenk H.-R. & Pernet M. (1997). Orientation analysis of bulk YBCO from incomplete neutron diffraction data. *J. Applied Crystallography*, **30**, 43-48.

Dimos D., Chaudhari P., Mannhart J. (1990). Superconducting transport properties of grain boundaries in $YBa_2Cu_3O_{7-d}$ bicrystals. *Physical Review B* **41(7)** 4038-4049.

Dimos D., Chaudhari P. (1988). Orientation dependence of grain-boundary critical currents in $YBa_2Cu_3O_{7-d}$ bicrystals. *Physical Review Letters* **61(2)** 219-222.

Drits V.A., Tchoubar C. (1990). "x-ray diffraction by disordered lamellar structures: theory and applications to microdivided silicates and carbons". Drits et Tchoubar Ed. Springer-Verlag 371p.

Du Xiao-Hong, Belegundu Uma, Uchino Kenji (1997). Crystal orientation dependence of piezoelectric properties in lead zirconate titanate: theoretical expectation for thin films. *Japanese J. of Applied Physics* **36** 5580-5587.

Elk K., Hermann R. (1993). Determination of texture and switching field of permanent magnetic materials by perpendicular rotational hysteresis investigations. *J. of Magnetism and Magnetic Materials* **128** 138-142.

Esling C., Muller J., H.-G. Bunge (1982). An integral formula expressing the even part $\widetilde{f}(g)$ in terms of f(g), or the apparition of the fn or fW ghost distributions. *J. de Physique* **43**, 189.

Falini Giuseppe, Albeck Shira, Weiner Steve, Addadi Lia (1996). Control of aragonite or calcite polymorphism by mollusk shell macromolecules. *Science* **271** 67-69.

Grasso G., Hensel B., Jeremie A. & Flükiger R. (1995). Distribution of the transport critical current density in Ag sheathed $(Bi,Pb)_2Sr_2Ca_2Cu_3O_x$ tapes produced by rolling. *Physica C* **241** 45-52.

Grenèche J.-M. (1981). Thèse de l'Université Pierre et Marie Curie, Paris 6. "Etude de propriétés magnétiques d'amorphes métalliques par spectrométrie Mössbauer". 110p.

Grenèche et Varret (1982). On the texture problem in Mössbauer spectroscopy. *J. of Physics C: Solid State Physics* **15** 5333-5344.

Heizmann, J.-J., Laruelle, C. (1986). Simultaneous measurement of several x-ray pole figures. *Journal of Applied Crystallography* **19**, 467-472.

Imhof J. (1982). The resolution of orientation space with reference to pole figure resolution. *Textures & Microstructures* **4**, 189-200.

Jin S., Graebner J.E. (1991). Processing and fabrication techniques for bulk high-Tc superconductors: a critical review. *Materials Sciences and Engineering* **B7** 243-260.

Kawasaki M., Sarnelli E., Chaudari P., Gupta A., Kussmaul A., Lacey J., Lee W. (1993). Weak link behavior of grain boundaries in Nd-, Bi-, and Tl-based cuprate superconductors. *Applied Physics Letters* **62(4)** 417-419.

Kocks, U.F., C. N. Tomé and H.-R. Wenk. 1998. *Texture and anisotropy: preferred orientations in polycrystals and their effect on materials properties*. Cambridge University Press, Cambridge. xii+676 pp.

Le Bail A. (1995). Modelling the silica glass structure by the Rietveld method. *J. of Non-Crystalline Solids* **183** 39-42.

Legrand B. (1996). "Texturation par solidification sous champ magnétique d'alliages samarium-cobalt. Application à l'élaboration d'aimants permanents massifs". Thèse de l'Université J. Fourier - Grenoble, France.

Liesert S. (1998). "Analyse physico-chimique des paramètres du développement d'une microstructure coercitive et anisotrope dans des poudres pour aimants liés puissants par application du procédé HDDR au Néodyme-Fer-Bore". Thèse de l'Université J. Fourier - Grenoble, France.

Lutterotti L., Matthies S., Wenk H.-R., Schultz A.S. and Richardson Jr. (1997). Combined Texture and structure analysis of deformed limestone from time-of-flight neutron diffraction spectra. *J. Applied Physics* **81**[2], 594-600.

Lutterotti L., Matthies S., Wenk H.-R. (1999). MAUD (Material Analysis Using Diffraction): a user friendly JAVA program for Rietveld Texture Analysis and more. In "Textures of Materials, vol. 2" (Ed J.A. Szpunar), NRC Research Press, Ottawa 1999, p1599-1604.

Matthies S. (1979). On the reproducibility of the Orientation Distribution Function of textured samples from pole figures (ghost phenomena). *Physica Status Solidi B* **92**, K135-K138.

Matthies S. & Humbert M. (1995). On the principle of a geometric mean of even-rank symmetric tensors for textured polycrystals. *Journal of Applied Crystallography* **28**, 254-266.

Matthies S., Lutterotti L. & Wenk H.-R. (1997). Advances in texture analysis from diffraction spectra. *J. Applied Crystallography* **30** 31-42.

Matthies S. & Vinel G.W. (1982). On the reproduction of the orientation distribution function of texturized samples from reduced pole figures using the conception of a conditional ghost correction. *Physica Status Solidi B* **112**, K111-K114.

Matthies S., Vinel G.W. & Helming K. (1987), "Standard distributions in texture analysis", Akademie-Verlag Berlin.

Matthies S., Wenk H.-R. (1985). ODF reproduction with conditional ghost correction. In "Preferred orientation in deformed metals and rocks : an introduction to modern texture analysis", H.-R. Wenk editor, Academic Press inc. pp 139-147.

Matthies S., Wenk H.-R. (1992): Optimization of texture measurements by pole figure coverage with hexagonal grids: *Physica Status Solidi A***133**, 253-257

Matthies S., Wenk H.-R. & Vinel G.W. (1988). Some basic concepts of texture analysis and comparison of three methods to calculate orientation distributions from pole figures. *J. of Applied Crystallography* **21**, 285-304.

Morales M., Artigas M., Bacmann M., Fruchart D., Skolozdra R., Soubeyroux J.-L., Wolfers P. (1999). Comparison of the magnetic properties of $ErMn_{12-x}Fe_x$ series with their related hydrides and carbides. *J. of Magnetism and Magnetic Materials* **196-197** 703-704.

Morales M., M. Artigas, M. Bacmann, D. Fruchart, P. Wolfers, B. Ouladiaff (2001a). Magnetic properties and interactions in the $RMn_{12-x}Fe_x$ series with R = Y, Ho, Er, Nd and $x \leq 8$. Submitted *European Journal of Solid State Inorganic Chemistry.*

Morales M., M. Bacmann, D. Fruchart, P. Wolfers, B. Ouladiaff (2001b). Impact of hydrogen and carbon insertion on the fundamental characteristics of the $ErMn_{12-x}Fe_x$ compounds. *Submitted J. Magnetism and Magnetic Materials*.

Pawlik K. (1993). Application of the EDC method for ODF approximation in cases of low crystal and sample symmetries. *Materials Science Forum* **133-136**, 151-156.

Pellerin N., Odier P., Simon P., Chateigner D (1994). Nucleation and growth mechanisms of textured YBaCuO: influence of Y_2BaCuO_5. *Physica C* **222** 133-148.

Ponder W.F., D.R. Lindberg (1997). Towards a phylogeny of gastropod molluscs: an analysis using morphological characters. *Zoological Journal of the Linnean Society* **119** 83-265.

Qun Wang, Zhi-gang Zhao, Wei Liu, Sun X.K., Chuang Y.C. (1992). Rotation alignment for measuring easy-plane magnetic anisotropy. *J. of Magnetism and Magnetic Materials* **109** 59-63.

Rivoirard S., D. Chateigner, P. de Rango, D. Fruchart, R. Perrier de la Bathie, J.-L. Soubeyroux (2000). Texture investigation of hot-forged Nd-Fe-B magnets. *Philosophical Magazine* A **80(8)**, 1955-1966.

Ruer D. (1976). "Méthode vectorielle d'analyse de la texture". Thèse Université de Metz, France.

Sandhage K.H. Jr., Riley G.N. & Carter W.L. 1991 J. Metals 43 21own single-domain $YBa_2Cu_3O_x$. *Applied Physics Letters* **70(26)** 3606-3608.

Schulz L.G. (1949a). Determination of preferred orientation in flat reflection samples using a Geiger counter x-ray spectrometer *J. Appl. Phys.* **20**, 1030-1033.

Schulz L.G. (1949b). Determination of preferred orientation in flat transmission samples using a Geiger counter x-ray spectrometer. *J. Appl. Phys.* **20**, 1033-1036.

Searle C.W., Davis V., Hutchens R.D. (1982). Magnetically determined particle alignement factors of sintered rare-earth cobalt permanent magnets. *J. Applied Physics* **53(3)** 2395-2397.

Soubeyroux J.-L., Fruchart D., O. Isnard, S. Miraglia, E. Tomey (1995). Role of the (H,C,N) intersticial elements on the magnetic properties of iron-rare earth permanent magnet alloys. *J. of Alloys and Compounds* **19** 16-24.

Swofford D.L., D.P. Begle (1993). *PAUP, Phylogenetic analysis using parsimony version 3.1, manual*. Laboratory of Molecular Systematics, Smithsonian Institution. 263 pp.

Von Dreele R.B. (1997). Quantitative texture analysis by Rietveld refinement. *J. of Applied Crystallography* **30** 517-525.

Waller T.R. (1998). Origin of the molluscan class Bivalvia and a phylogeny of major groups. In: *Bivalves: an eon of evolution - paleobiological studies honoring Norman D. Newell*, P.A. Johnston and J.W. Huggart, eds. pp. 1-45. University of Calgary Press, Calgary.

Wang Y.D., Zuo L., Liang Z.D., Laruelle C., Vadon A., Heizmann J.-J. (1997). Quantitative texture analysis from x-ray diffraction spectra. *J. of Applied Crystallography* **30** 443-448.

Weiner S. & Traub W. (1980). X-ray diffraction study of the insoluble organic matrix of mollusk shells. *FEBS Letters* **111**(**2**) 311-316.

Weiner Stephen & Traub Wolfie (1981). Organic-Matrix-Mineral relationships in mollusk-shell nacreous layers. "*Structural aspects of recognition and assembly in biological macromolecules*" M. Balaban, J.L. Sussman, W. Traub and A. Yonath Eds. Balaban ISS, Rehovot and Philadelphia. P467-482.

Wenk H.-R. (1992). Advantages of monochromatic x-rays for texture determination of superconducting thin films. *J. of Applied Crystallography* **25**, 524-530.

Wenk H.-R., Heidelbach F., Chateigner D. & Zontone F. (1997). Laue orientation imaging. *J. Synchrotron Radiation* **4** 95-101.

Wenk H.-R., Matthies S., Donovan J., Chateigner D. (1998). BEARTEX: A Windows based program for quantitative texture analysis. *Journal of Applied Crystallography* **31**, 262-269.

Wenk H.-R., Matthies S., Lutterotti L. (1994). Texture analysis from diffraction spectra. *Materials Science Forum* **157-162** 473-479.

Wenk H.-R., Pawlik K., Pospiech J., Kallend J.S. (1994). Deconvolution of superposed pole figures by discrete ODF methods: comparison of ADC and WIMV for quartz and calcite with trigonal crystal and triclinic specimen symmetry. *Texture & Microstructure* **22** 233-260.

Wright Stuart I. (1993). A review of automated orientation imaging microscopy (OIM). *J. of Computer-Assisted Microscopy* **5(3)** 207-221.

Wright Stuart I., Adams Brian L. (1992). Automatic analysis of electron backscatter diffraction patterns. *Metallurgical transactions A, Physical metallurgy and materials science* **23(3)** 759-767.

Yan A-ru, Zhang Wen-yong, Zhang Hong-wei, Shen Baogen (2000). Melt-spun magnetically anisotropic $SmCo_5$ ribbons with high permanent performance. *J. of Magnetism and Magnetic Materials* **210**, L10-L14.